Journal of Catalysis 348 (2017) 75–89

Contents lists available at ScienceDirect

Journal of Catalysis

journal homepage: www.elsevier.com/locate/jcat

Kinetic and spectroscopic evidence for reaction pathways and intermediates for olefin epoxidation on Nb in *BEA

Daniel T. Bregante, Pranjali Priyadarshini, David W. Flaherty *

Department of Chemical and Biomolecular Engineering, University of Illinois Urbana-Champaign, Urbana, IL 61801, United States

ARTICLE INFO

Article history:
Received 22 December 2016
Revised 19 January 2017
Accepted 12 February 2017

Keywords:
Olefin epoxidation
Zeolites
Niobium
In situ spectroscopy
Metal oxide catalysis
Green chemistry
Hydrogen peroxide

ABSTRACT

The selective epoxidation of olefins with hydrogen peroxide (H_2O_2) over transition metal substituted zeolites is less environmentally impactful than epoxidation schemes that use chlorinated or organic oxidants. The structure and reactivity of reactive intermediates derived from H_2O_2 and the mechanism for olefin epoxidation on such materials are debated. Here, cyclohexene oxide formation and H_2O_2 decomposition rates (measured as functions of reactant and product concentrations) and in situ infrared (IR) and UV-vis spectroscopy are used to probe the intervening elementary steps for cyclohexene (C_6H_{10}) epoxidation and the identity of the reactive intermediates on a Nb-β catalyst. IR and UV-vis spectra acquired in situ show that the reactive intermediates are predominantly superoxide species (Nb^{IV}-$(O_2)^-$, observed also by X-ray photoelectron spectroscopy), which form by the irreversible activation of H_2O_2 over Nb centers. Similar M-$(O_2)^*$ (M = Ti or Ta) intermediates were previously assumed to form via reversible processes; however, in situ IR and UV-vis measurements directly show that Nb^{IV}-$(O_2)^-$ forms irreversibly in both H_2O and acetonitrile. Activation enthalpies ($\Delta H^{\ddagger}$) for C_6H_{10} epoxidation are 27 kJ mol^{-1} higher than for H_2O_2 decomposition, while activation entropies ($\Delta S^{\ddagger}$) for epoxidation are 56 J mol^{-1} K^{-1} lower than for H_2O_2. These comparisons show that the selectivities for epoxidation, via primary reaction pathways, increase with increasing reaction temperatures. Collectively, these results provide a self-consistent mechanism for C_6H_{10} epoxidation that is also in agreement with previously published data. These findings will aid the rational design and study of alternative metal oxide catalysts for olefin oxidation reactions.

1. Introduction

Epoxides are important precursors for the synthesis of epoxy resins, plastics, and complex molecules used to manufacture aircraft hulls, perfumes, and pharmaceuticals [1–3]. Currently, epoxides are produced primarily by the reaction of olefins with stoichiometric amounts of organic peroxy compounds [4] or through chlorohydrin intermediates followed by strong alkaline treatments to form oxiranes [5,6]. These processes generate stoichiometric amounts of corrosive organic acids and alcohols [7] or chloride salts [5], respectively, that require subsequent energy-intensive separation, waste treatment, and regeneration [8,9]. More environmentally benign oxidants should be used; however, the costs of "green" oxidants that generate less waste are generally greater and the product selectivities may be lower than Cl-mediated pathways [10,11]. Hydrogen peroxide (H_2O_2) is one such oxidant whose use only by-product in epoxidation reactions is water (H_2O), which is easily separated from organic product streams by liquid-liquid extraction [12,13]. Currently, the high relative cost of H_2O_2 (to that of Cl-based oxidizers) requires catalysts that selectively activate and utilize H_2O_2 for olefin epoxidation while minimizing non-productive H_2O_2 decomposition (i.e., $2H_2O_2 \rightarrow O_2 + 2H_2O$) and epoxide decomposition.

Isolated metal centers and small oligomers of early transition metal oxides (e.g., Al^{III} [14,15], Ti^{IV} [7,16–18], Zr^{IV} [19,20], Ta^{V} [21–23], and Nb^{V} [24,25]) catalyze the epoxidation of olefins with H_2O_2. Isolated Nb atoms grafted onto silica give greater rates and selectivities for olefin epoxidation compared to isolated Ti centers as well those of other groups IV and V metals (i.e., Zr, Hf, V, and Ta) on silica, which was attributed to differences between the Lewis acidity (estimated from the ionic character of the M-O bond) of the different metal atoms [20]. Zeolite frameworks can stabilize relatively high loadings of isolated transition metal atoms [26–30], which in some cases, are believed to possess higher turnover rates ((mol product)(mol active site·s)$^{-1}$) and selectivities than their oligomeric- and bulk-oxide counterparts. For example, Ti centers in titania silicalite (TS-1) activate H_2O_2 to form

* Corresponding author.
E-mail address: dwflhrty@illinois.edu (D.W. Flaherty).

http://dx.doi.org/10.1016/j.jcat.2017.02.008
0021-9517/

intermediates that epoxidize propylene in one of few industrially practiced H_2O_2-based oxidation reactions [31–33]. TS-1, however, possesses relatively small diameter pores (~5 Å, due to the MFI framework) [34], which hinders the diffusion of larger olefins (e.g., cyclooctene, limonene) [31,35] to Ti centers within the pores. Larger pore zeolite frameworks, such as the beta (*BEA) polymorph, possess pores with diameters of ~7 Å [34], which broadens the range of potential substrates for epoxidations [36]. Post-synthetic modification of *BEA and other zeolites provides a facile method to synthesize transition metal substituted catalysts using commercially-available zeolites as precursors [26,27,36,37], which enables studies of how the elemental identity of isolated metal centers in similar coordination environments affects catalysis [38]. As such, the mechanism of olefin epoxidation on transition metal substituted *BEA (M-β) must be established before such periodic trends can be understood.

Here, we combine catalytic rate measurements with in situ UV-vis and Fourier transform-infrared (FTIR) spectra to determine the mechanism for cyclohexene epoxidation and the structure and reactivity of relevant reaction intermediates on Nb-β. In situ UV-vis and IR spectroscopy show Nb-bound superoxide (Nb^{IV}-$(O_2)^-$) and hydroperoxide/peroxide (Nb^{V}-OOH and Nb^{V}-$(O_2)^{2-}$) intermediates form by irreversible activation of H_2O_2 at Nb-atoms, which conflicts with proposed mechanisms for olefin epoxidation on similar catalysts (i.e., TS-1 [39], Ta-SBA-15 [21,40], and Ta-SiO_2 [22,23]) that assume reversible (and quasi-equilibrated) H_2O_2 activation. X-ray photoelectron spectroscopy of H_2O_2-activated Nb-β confirms the presence of Nb^{IV}-$(O_2)^-$ surface species by showing that Nb atoms shift from a 5+ to 4+ oxidation state when activated with H_2O_2. A combination of transient in situ UV-vis and FTIR measurements demonstrates that the Nb^{IV}-$(O_2)^-$ specie is the active oxidizing intermediate for epoxidation and possesses a rate constant for epoxidation that is a factor of $2 \cdot 10^4$ larger than that for Nb^{V}-OOH/Nb^{V}-$(O_2)^{2-}$.

Turnover rates ((mol product)(mol Nb atom·s)$^{-1}$) were measured as functions of the concentrations of C_6H_{10} (0.01–5 M), H_2O_2 (0.5–5 mM), and cyclohexene oxide ($C_6H_{10}O$, 1–5 mM). Formation rates of $C_6H_{10}O$ increase in proportion to $[C_6H_{10}]$ but become constant at high $[C_6H_{10}]$ values. The rate of epoxidation is independent of $[H_2O_2]$ when $[C_6H_{10}]$ is low, but becomes proportional to $[H_2O_2]$ at high $[C_6H_{10}]$. These results reflect the competitive adsorption of H_2O_2- and C_6H_{10}-derived species, which results in a change in the most abundant reactive intermediate (MARI) on Nb-sites. Upon formation of Nb^{IV}-$(O_2)^-$, the intermediate reacts with either C_6H_{10} or H_2O_2 to form the epoxidation (i.e., cyclohexene oxide) or decomposition products (i.e., H_2O and O_2), respectively. Measured activation enthalpies ($\Delta H^{\ddagger}$) for epoxidation (72 kJ mol^{-1}) and H_2O_2 decomposition (45 kJ mol^{-1}) show that decomposition is enthalpically favorable, whereas activation entropies ($\Delta S^{\ddagger}$, −35 J mol^{-1} K^{-1} for $C_6H_{10}O$ formation and −91 J mol^{-1} K^{-1} for H_2O_2 decomposition) suggest that epoxidation is entropically favorable. Collectively, these data provide insight as to the identity of the reactive surface species responsible for epoxidations and the mechanism for this reaction on transition metal substituted zeolites, which is needed to understand the underlying chemical reasons that lead to significant differences in rates and selectivities that reflect the elemental identity of the transition metal atoms that facilitate oxidation reactions.

2. Methods and material characterization

2.1. Synthesis of Nb-β catalysts

Niobium-substituted zeolite catalysts were prepared by the post-synthetic modification of commercial zeolite beta [26,27]. Commercial *BEA (Zeolyst, Si:Al ~ 12.5, NH_4^+ cation, Al-β) was dealuminated by treatment with concentrated HNO_3 (Macron Chemicals, 69–70 wt.%, 20 cm^3 per gram of zeolite) at reflux (448 K) for 20 h. Slurries of Al-β and HNO_3 are initially a dark brown color, but the colors of these suspensions change to a light tan after four hours at reflux. The dealuminated zeolite (Si-β, Si:Al > 1200 determined by inductively couple plasma – optical emission spectroscopy) was then recovered by filtration and washed with concentrated HNO_3 (10 cm^3 g^{-1}) followed by deionized (DI) water (17.8 MΩ, 20 cm^3 g^{-1}). The wet recovered Si-β solids were dried in an oven within ambient air for 18 h at 423 K. The dried solids were then heated to 823 K at 5 K min^{-1} and held at 823 K for 6 h in flowing dry air (Airgas, Ultra-zero grade, 100 cm^3 min^{-1}) with the intent to remove residual organics from the Si-β. Nb atoms were incorporated into the framework by liquid-phase adsorption (LPA), which involved stirring Si-β in a 0.35–3.5 mM solution of $NbCl_5$ (Sigma-Aldrich, 99%, 50 cm^3 g^{-1}) in isopropyl alcohol (VWR Analytical, >99.5%) for 6 h at 343 K. Volatiles were then removed in vacuo at 6.6 kPa for 30 min followed by washing with 75 cm^3 g^{-1} DI water with the intent to remove any residual $NbCl_5$ not exchanged into defects within the framework. The recovered solids were heated to 723 K at 5 K min^{-1} and held at 723 K for 4 h in flowing dry air (Airgas, Ultra-zero grade, 100 cm^3 min^{-1}) to yield a white powder. Nb-substituted zeolites are referred to as Nb_x-β where the subscript denotes the final wt.% of Nb (0.15–5.0 wt.%), which was controlled by changing the concentrations of $NbCl_5$ and Si-β in the LPA solution.

A 10 wt.% Nb-SiO_2 (Nb_{10}-SiO_2) catalyst was prepared by incipient wetness impregnation of washed SiO_2 (1 g, Sigma–Aldrich, Davisil 646, 35–60 mesh) with 1.2 cm^3 of 0.898 M $NbCl_5$ dissolved in isopropyl alcohol. The catalyst was dried under ambient conditions for 4 h by ramping to 823 K (5 K min^{-1}) for 6 h under flowing dry air (Airgas, Ultra-zero grade, 100 cm^3 min^{-1}).

2.2. Catalyst characterization

Catalyst metal loadings were quantified using inductively coupled plasma optical emission spectroscopy (ICP-OES, PerkinElmer 2000DV), calibrated against known dilution standards. The reported Nb_x-β subscript corresponds to values measured by ICP-OES.

Catalyst crystallinity was confirmed by powder X-ray diffraction (p-XRD). X-ray diffractograms were obtained using a powder X-ray diffractometer (Siemens/Bruker D-5000) with Cu K-α radiation (0.15418 nm) using a step size of 0.02° at 1° min^{-1} in an ambient atmosphere. X-ray diffractograms for commercial NH_4^+-β, the dealuminated Si-β, and prepared Nb-β catalysts are effectively indistinguishable (Fig. S1). These comparisons show that the post-synthetic modification method does not affect the crystalline structure of the zeolites, and that framework crystallinity is maintained.

Diffuse reflectance UV-vis (DRUV-vis) spectra were measured from 700 to 175 nm using a spectrophotometer (Agilent CARY 5 UV-vis-NIR) equipped with a diffuse-reflectance accessory (Harrick Cricket®). Spectra were recorded in absolute reflectance (R) mode at ambient pressure and temperature. Magnesium oxide powder (MgO, Sigma Aldrich, 99.995% trace metals basis) or a polished gallium mirror (Harrick Cricket®) was used to collect a total reflectance spectrum for use as a baseline for Kubelka-Munk pseudo absorbances (Fig. S2). Nb-β and Nb-SiO_2 samples were ground with MgO (10% sample by weight) prior to measurement. Optical band gaps (E_g) were calculated from the x-intercept of the linear portion of a Tauc plot (Fig. S3) [20,41]. Table 1 summarizes the optical band edges of Nb-β, Nb_{10}-SiO_2, bulk Nb_2O_5 [42], and calixarene-assisted Nb grafted onto silica (Calix-$Nb_{1.7}$-SiO_2) [20]. Nb_{10}-SiO_2 has a band edge (3.7 eV) that is similar to that of bulk Nb_2O_5 (3.4 eV) [42],

Table 1
Optical band edges and wavelengths of maximum absorption obtained from diffuse-reflectance UV-vis spectroscopy Nb-based catalysts. Catalysts were mixed with MgO in a 1:10 ratio by weight prior to measurement under ambient conditions. Pure MgO was used as the reference material.

Sample	Band edge (eV)	Maximum absorption (nm)
Bulk Nb_2O_5	3.4 [42]	–
$Nb_{10.0}$-SiO_2	3.7	–
Calix-$Nb_{1.7}$-SiO_2	4.0 [20]	240
$Nb_{0.7}$-β	4.2	255
$Nb_{1.5}$-β	4.2	255

which indicates that this material contains metal-oxide clusters with bulk-like electronic properties and sizes of at least several nanometers. All Nb-β catalysts have band edge energies (4.2 eV) that are much larger than that of bulk Nb_2O_5 and similar to those previously reported (4.0 eV) for isolated atoms grafted onto mesoporous silica [20]. The similarity between the band gaps for $Nb_{0.7}$-β and $Nb_{1.5}$-β strongly suggests that Nb atoms are incorporated into the zeolite framework as single isolated sites (i.e., the samples contain immeasurable extents of Nb-O-Nb connectivity). If the Nb atoms were not incorporated into the zeolite framework, but rather forming small clusters, the NbO_x clusters would become larger with increasing loadings, which would result in a decreasing band gap. Additionally, Fig. S2 shows the Kubelka-Munk absorbance as a function of wavelength for $Nb_{0.7}$-β, $Nb_{1.5}$-β, and Nb_{10}-SiO_2. Both Nb-β samples show no distinct absorbance feature beyond ~300 nm, which suggests that no extra-framework Nb^V species exist as either bulk or oligomeric niobia-like phases [26,43].

Solid-state magic angle spinning-nuclear magnetic resonance (MAS NMR) spectroscopy was performed on a spectrometer (Varian, Unity Inova 300 MHz) equipped with a 4 mm MAS probe (Varian-Chemagnetics, double resonance APEX HX). Approximately 36.4 mg of $Nb_{1.5}$-β was packed into a 4 mm zirconia rotor, which was spun at 10 kHz in the spectrometer for MAS-NMR. Powdered octakis(dimethylsilyloxy)silsesquioxane (Q_8M_8) was used for pulse calibration and ^{29}Si chemical shift referencing (Q_8M_8 has a chemical shift of 11.45 ppm, relative to the primary standard, tetramethylsilane at 0 ppm). ^1H direct polarization (DP-MAS NMR) was performed with a 10 s recycle delay with the averaging of 32 scans. $^1H \rightarrow {}^{29}Si$ cross polarization (CP-MAS NMR) was performed with a 5 s recycle delay using an 8 ms contact time with the averaging of 6000 scans. ^{29}Si DP-MAS NMR was performed with a 10 s recycle delay with the averaging of 6000 scans. ^{93}Nb MAS NMR experiments were unsuccessful due to low signal to noise levels even with 69,000 scans with a 1 s recycle delay.

Fig. S4 shows ^1H MAS-NMR spectra for $Nb_{1.5}$-β. The lack of a distinct feature located at 5.4 ppm is consistent with the incorporation of Nb atoms into silanol pockets during post-synthetic modification [43]. Fig. S5a shows the ^{29}Si DP-MAS NMR spectra for $Nb_{1.5}$-β, which shows three distinct features at −102, −112, and −115 ppm. The feature at −102 ppm is attributed to Si atoms in a $Si(OH)(OSi)_3$ environment [43–45], while the features at −112 and −115 ppm are assigned to Si atoms in a $Si(OM)_4$ environment, where M = Si or Nb, which are similar to features seen in Nb-β [43], Ta-β [45], and Zr-β [44]. Fig. S5b shows the $^1H \rightarrow {}^{29}Si$ CP-MAS NMR spectra with an 8 ms contact time, which is used to selectively enhance the excitation of Si atoms that are near ^1H atoms. Fig. S5b clearly shows the enhancement of the feature located at −102 ppm during cross polarization, which confirms the assignment of this feature to $Si(OH)(OSi)_3$ atoms. In short, the appearance of the −112 and −115 ppm features in Fig. S5a suggests that the Nb atoms are incorporated into the framework as there are two distinct type of Q4 Si atoms (i.e., $Si(OM)_4$), and these features are similar to those observed in related framework-substituted *BEA (i.e., Nb-β [43], Ta-β [45], and Zr-β [44]).

Nb-atom incorporation was also characterized by attenuated total reflectance IR spectroscopy (ATR-IR, Bruker Alpha). $Nb_{1.5}$-β and Si-β samples (~10 mg) were pressed onto a diamond ATR-IR internal reflection element and IR spectra were recorded (32 scans, 2 cm^{-1} resolution) at ambient conditions. Fig. S6a shows IR spectra for Si-β and $Nb_{1.5}$-β samples just after heating to 823 K for 6 h in flowing air (100 $cm^3\ min^{-1}$, Praxair, Ultra-zero grade), both of which exhibit absorbance features centered at 1234, 1075, and 803 cm^{-1}, which correspond to the SiO_4 internal tetrahedral stretch, the ν_{as}(Si-O), and the ν_s(Si-O) features, respectively [46]. $Nb_{1.5}$-β also possesses an additional feature in the ATR-IR spectra that is centered at 950 cm^{-1} (Fig. S6c), which corresponds to ν(Si-O-Nb) [43,47]. Additionally, extra-framework Nb atoms would result in a distinct absorbance feature at ~835 cm^{-1} which is assigned to ν_s(O-Nb-O) of oligomeric or polymeric niobia [48]. Fig. S6d shows the difference spectra for $Nb_{10.0}$-SiO_2 with respect to SiO_2, and possesses a distinct absorbance feature at 831 cm^{-1}, which suggests that $Nb_{10.0}$-SiO_2 contained oligomeric or bulk-like clusters of niobia on the surface. Notably, the lack of an additional IR absorbance feature (Fig. S6c) near 835 cm^{-1} suggests that these Nb-β samples do not contain oligomeric or bulk forms of NbO_x. These data, in conjunction with DRUV-vis and solid-state NMR, strongly suggest that Nb atoms have been incorporated into the *BEA framework and that no extra-framework Nb^V is formed after the post-synthetic modification of *BEA.

The presence of Lewis acid sites was characterized by the FTIR spectroscopy of deuterated acetonitrile (CD_3CN, Cambridge Isotope Laboratories, 99.8% D atom) [49,50] coordinated to $Nb_{1.5}$-β and Si-β using a custom-made transmission cell, the design of which was described previously [51]. The transmission cell was mounted within an FTIR spectrometer (Bruker, Tensor 37) equipped with a liquid-N_2 cooled HgCeTe detector. Catalysts were pressed into self-supporting wafers (~80 mg) and placed within the stainless-steel cell, which was equipped with CaF_2 windows and connected to a gas manifold by gas-transfer lines that were heated to 423 K via electrical heating tape (Omega, FGH Series). The catalyst temperature was measured using a K-type thermocouple (Omega) located within the cell. Catalysts were heated to 423 K at 10 K min^{-1} and held at 423 K for 1.5 h under flowing He (50 $cm^3\ min^{-1}$, Airgas, Ultra High Purity) to remove H_2O and then allowed to cool to 298 K. Liquid CD_3CN (1 μL min^{-1}) was fed via a syringe pump (Legato 100, KD Scientific) and vaporized inside the heated gas-transfer lines into a stream of flowing He (50 $cm^3\ min^{-1}$) to generate a mixture (1.2 kPa CD_3CN, 100 kPa He). Each catalyst was then contacted with the CD_3CN/He stream until reaching the saturation coverage of CD_3CN (determined by constant absorbance intensities in FTIR spectra, ~15 min) at which point the CD_3CN flow was stopped. The sample was then heated at 10 K min^{-1} to increasing temperatures in 20 K increments to a maximum temperature of 423 K, and steady-state FTIR spectra (128 scans, 1 cm^{-1} resolution) were acquired continuously.

Fig. 1 shows representative FTIR spectra for CD_3CN adsorbed on Si-β (Fig. 1a) and $Nb_{1.5}$-β (Fig. 1b). Absorption features between 2260 and 2340 cm^{-1} correspond to the ν(C≡N) mode, while the band near 2115 cm^{-1} arises from the $\delta_s(CD_3)$ mode [50]. The absorbance peak located at 2275 cm^{-1} (Fig. 1a) is associated with CD_3CN hydrogen bonded to silanol groups located within the zeolite, while the shoulder located at 2265 cm^{-1} is attributed to physisorbed CD_3CN, which weakly interacts with the pore walls [50]. As the temperature of the Si-β sample increases, hydrogen-bonded CD_3CN species (2275 cm^{-1}) persist on the surface, while the physisorbed CD_3CN (2265 cm^{-1}) desorb. Spectra of CD_3CN on $Nb_{1.5}$-β (Fig. 1b, 298 K) largely resemble those of Si-β but possess an additional absorption feature at 2306 cm^{-1} that can be

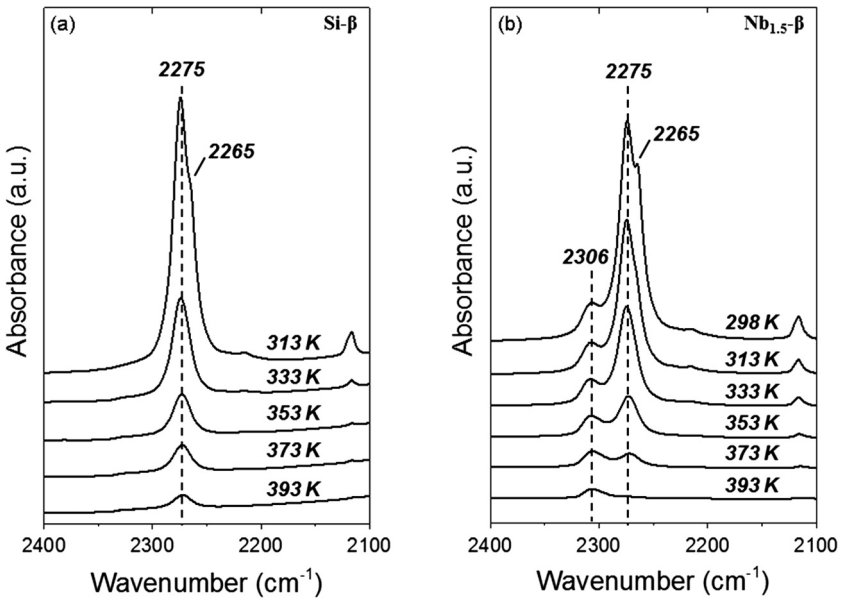

Fig. 1. Infrared spectra of adsorbed CD_3CN on the (a) Si-β and (b) $Nb_{1.5}$-β samples at the indicated temperatures within a steam of flowing He (101 kPa). Prior to the acquisition of these spectra, the samples were saturated with CD_3CN at 298 K (1.2 kPa CD_3CN, 100 kPa He, 50 cm^3 min^{-1}), after which CD_3CN flow was stopped.

attributed to Lewis acid sites associated with adsorption on Nb atoms, similar to CD_3CN features on Sn-β [49]. Yet these spectra on $Nb_{1.5}$-β show only a single new feature, in contrast to FTIR spectra of CD_3CN on Sn-β, which show features at both 2308 and 2316 cm^{-1} and reflect the presence of both open and closed Lewis acid sites [49]. Consequently, we conclude that $Nb_{1.5}$-β possesses predominantly one type of Lewis acid site, because additional types of Lewis acid sites would result in multiple absorbance peaks in the 2300 cm^{-1} region [52]. These results (Fig. 1) taken together with NMR spectra (Figs. S4 and S5) strongly suggest that the Lewis acid sites are Nb-atoms tetra-coordinated within the zeolite framework [52].

The UV-vis (Figs. S2 and S3), solid-state NMR (Figs. S4 and S5), and ATR-IR (Fig. S6) data show that Nb atoms are incorporated into the *BEA framework and do not exist as extra-framework bulk or oligomeric niobia. Additionally, the IR spectra of adsorbed CD_3CN (Fig. 1b) show a single absorbance feature associated with Lewis acidic sites. It is possible that multiple types of Nb sites exist in Nb-β, that have similar IR absorption features for adsorbed CD_3CN and also possess similar heats of adsorption that preclude their detection; however, this seems to be unlikely due to the significant shift in wavenumbers (2308 and 2316 cm^{-1}) and different heats of adsorption seen in Sn-β for open and closed sites [49]. These Lewis acid sites are most likely to be Nb atoms tetra-coordinated to the framework of β and to possess a single pendant —OH (i.e., Nb $(OSi)_4(OH)$) based on the characterization here, together with previous results that combined experiments (i.e., solid-state NMR, powder XRD, UV-vis, XPS, and IR spectroscopy) and theory (i.e., ab initio DFT calculations) to show that the most energetically stable form of Nb in Nb-β is the $Nb(OSi)_4(OH)$ unit [26,43].

X-ray photoelectron spectroscopy (XPS) measurements were used to measure the oxidation state of Nb atoms in $Nb_{5.0}$-β and H_2O_2-activated $Nb_{5.0}$-β (Section 2.4) and were performed on a Kratos AXIS Ultra spectrometer with a monochromatic Al-Kα (1486.6 eV) X-ray source. High-resolution spectra were collected with 40 eV pass energy, and the binding-energy scales were referenced with respect to the aliphatic C 1 s absorbance feature at 284.8 eV. Peak fittings were done in CasaXPS© via the method of Shirley.

2.3. Epoxide formation and H_2O_2 consumption rate measurements

Reaction rates for epoxidation were measured using a batch reactor (100 cm^3, three-neck round bottom flask) equipped with a reflux condenser to minimize evaporative losses. For typical reaction conditions, the reactor was filled with a solvent mixture of ~30 cm^3 acetonitrile (CH_3CN, Macron Chemicals, >99.8%) and 30 μL benzene (Sigma-Aldrich, thiophene free, >99%) as an internal standard. The reagents, C_6H_{10} (Sigma-Aldrich, >99%) or cis-stilbene (Sigma-Aldrich, >96%) and H_2O_2 (Fischer Chemicals, 30 wt.% in H_2O), were added and the reaction mixture was heated to the desired temperature (303–333 K) while stirring at 450 rpm. The epoxidation of C_6H_{10} was initiated by introducing ~30 mg of the Nb-β catalyst. Small aliquots (~300 μL) were extracted through a 0.22 μm filter (GS-Tek, PVDF filter) to remove suspended catalyst, and thus quench C_6H_{10} epoxidation and H_2O_2 decomposition. All reactants and solvents used were miscible under the conditions tested in this study. The concentrations of $C_6H_{10}O$ and other potential reaction products (e.g., cyclohexane diol and cyclohexanol) were determined as a function of time with a gas chromatograph (HP-5890 Series A) equipped with a non-polar dimethylpolysiloxane capillary column (Agilent, HP-1, 30 m length, 1.05 μm) and a flame ionization detector. All species were identified and response factors were calculated using calibrated mixtures of known standards. The change in the concentration of H_2O_2 was determined by colorimetric titrations using a solution of Cu-based indicator (12 mM neocuproine (Sigma-Aldrich, >98%); 8.3 mM $CuSO_4$ (Fisher Chemicals, >98.6%); 25% v/v ethanol (Decon Laboratories Inc., 100%)) [53,54]. The concentration of H_2O_2 in each aliquot was determined from the absorbance at 454 nm, measured using a visible-light spectrophotometer (Spectronic, 20 Genesys), and by comparison to calibrated standards. In all reported data, the selectivity toward $C_6H_{10}O$ formation was >99% (e.g., no common byproducts were detected, such as cyclohexanol or cyclohexane diol) upon reaction of C_6H_{10} with H_2O_2 over Nb-β. The carbon balance closed to within 98% for all reactions reported, which shows all significant reaction products were detected. The calculated uncertainties for all turnover rate measurements are less than 7%, as determined by comparison of repeated measurements.

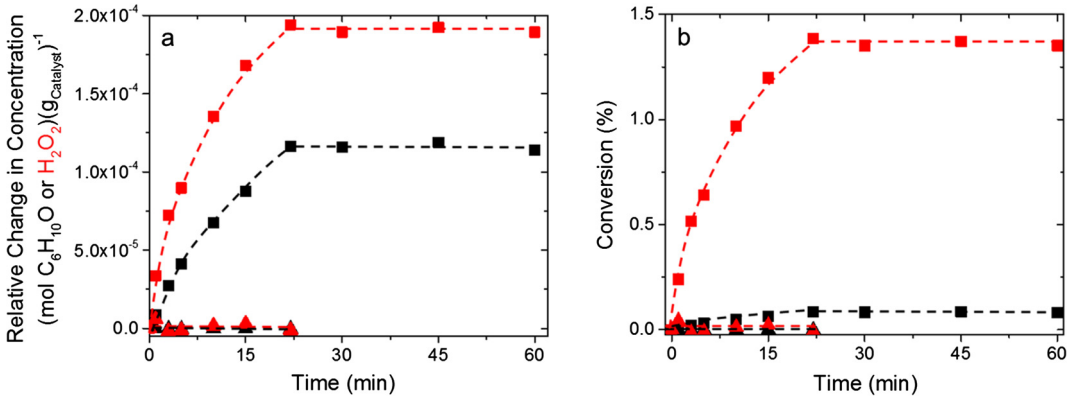

Fig. 2. Concentration profiles for the formation of $C_6H_{10}O$ (black) and for the consumption of H_2O_2 (red) as a function of time expressed as (a) Relative Change in Concentration (given in mol $(g_{cat})^{-1}$) for direct comparison between catalysts, as there is no Nb present in Si-β, and (b) conversion of C_6H_{10} (taken as $(mol_{C_6H_{10}O})(mol_{C_6H_{10},initial})^{-1}$) or H_2O_2 (10 mM C_6H_{10}, 1 mM H_2O_2, $Nb_{1.5}$-β (■) or Si-β (▲) in CH_3CN, 313 K) with hot filtration at 22 min. Lines are intended to guide the eye.

Control experiments were performed using Si-β and $Nb_{1.5}$-β to demonstrate that the metal centers contained within the zeolite were responsible for C_6H_{10} epoxidation and H_2O_2 consumption. Fig. 2 shows that turnover numbers (TON) for C_6H_{10} epoxidation and H_2O_2 consumption are undetectable on Si-β but increase with time on $Nb_{1.5}$-β, which shows that the Nb atoms in the framework catalyze epoxidation and H_2O_2 conversion. The values of the TON become constant (i.e., turnover rates are zero) after hot filtration, suggesting that Nb-atoms do not leach into solution and homogeneously catalyze epoxidation. Additionally, ICP-OES analyses of the reaction solution (after 1 h of reaction) and of the spent $Nb_{1.5}$-β show no discernible changes in the Nb content of either the liquid phase or the solid catalyst. The ICP-OES analysis performed has an experimental error of ±0.01 wt.%, which correlates to a sensitivity of <1% of the total Nb content of the catalyst. Turnover rates reported in all subsequent sections were obtained in the linear region (i.e., first 5 min) of olefin epoxidation at differential conversion (i.e., <5% conversion of C_6H_{10} and H_2O_2).

Reported rates of C_6H_{10} epoxidation and H_2O_2 consumption were measured in the absence of mass-transfer limitations. To ensure that the Madon-Boudart criterion [55] was satisfied, reactions were performed with Nb-β catalysts with different metal loadings (0.15–1.5 wt.% Nb) at constant H_2O_2 concentrations over a range of C_6H_{10} concentrations (Section S2, Fig. S8). Epoxidation turnover rates did not depend on the Nb content over this range of weight loadings, which shows that intra-pellet mass-transfer limitations were insignificant. Reported turnover rates and kinetic analyses are taken from experiments using $Nb_{1.5}$-β.

2.4. Activation of Nb-β with H_2O_2 for XPS analysis

$Nb_{5.0}$-β (200 mg) was combined with a mixture of 2.5 cm^3 CH_3CN and 2.5 cm^3 H_2O_2 (30 wt.% in H_2O) to produce H_2O_2-activated $Nb_{5.0}$-β for XPS analysis of the Nb oxidation states. The $Nb_{5.0}$-β changed from bleached white to pale yellow in color upon addition of the H_2O_2-CH_3CN mixture. This slurry was then heated to 333 K for 1 h with the intent of reacting all of the Nb active sites with H_2O_2 in solution. The slurry was then dried under dynamic vacuum (5.3 kPa) at 333 K for 30 min followed by static vacuum (0.02 kPa) for 12 h, which gave the final H_2O_2-activated $Nb_{5.0}$-β material (light yellow solid).

2.5. In situ UV-vis and IR spectroscopy

In situ UV-vis spectroscopy was used to measure the reactivity of the different intermediates for epoxidation on Nb-β. $Nb_{0.3}$-β samples were pressed into 7 mm diameter self-supporting pellets (~5 mg) and loaded into a custom-built UV-vis liquid flow cell. Reactant and solvent solutions were introduced using a high-performance liquid chromatography (HPLC) pump (Waters, 515), and UV-vis spectra were collected using a 45-degree reflection probe (Avantes, solarization-resistant fibers) attached to an Ava-Fast fiber-optic spectrometer (Avantes 2048) with a compact deuterium-halogen light source (Avantes, 200–1700 nm). The $Nb_{0.3}$-β samples were activated by flowing (1 cm^3 min^{-1}) a solution of H_2O_2 in CH_3CN (0.1 M H_2O_2, 0.4 M H_2O) over the pellet at 313 K until the absorbance features at ~320 nm were unchanging (~15 min). A H_2O_2-free solution of CH_3CN (0.4 M H_2O) then flowed through the reactor (1 cm^3 min^{-1}) to remove all liquid-phase and weakly adsorbed H_2O_2 from the system at 313 K. This treatment did not attenuate the UV-vis absorbance features, which shows that the surface species on H_2O_2-activated $Nb_{0.3}$-β were stable at 313 K under pure CH_3CN. The reactivity of the surface intermediates on $Nb_{0.3}$-β was measured by continuously acquiring UV-vis spectra (600 ms integration time, co-adding 100 scans per spectrum) while flowing a solution of C_6H_{10} in CH_3CN (0.1 M C_6H_{10}, 0.4 M H_2O), similar to that used for rate measurements in the batch reactor. Reference spectra for all experiments were obtained using a $Nb_{0.3}$-β pellet within a flowing CH_3CN solution (0.4 M H_2O) at 313 K. Peak smoothing, background subtraction, and spectral deconvolution were performed in OriginPro® (Section S3.1 for example spectra).

In situ attenuated total reflectance infrared (ATR-IR) spectroscopy was used to characterize the vibrational structure and chemical stability of the intermediates formed upon exposing Nb-β to H_2O_2. Untreated $Nb_{1.5}$-β was deposited onto a ZnSe cylindrical internal reflection element (IRE, International Crystal Labs) by dip coating. Briefly, 100 mg of $Nb_{1.5}$-β was suspended in ~10 cm^3 of CH_3OH (Macron Chemicals, anhydrous) and the IRE was dipped into the suspension and subsequently dried at ambient temperature to retain the powdered catalyst on the IRE. A series of 10 cycles were typically used to accumulate a thin layer of $Nb_{1.5}$-β. The catalyst-coated IRE was then loaded into a customized ATR flow cell (Axiom TNL-120) equipped with two liquid inlets and one outlet with a cell volume of 40 μL. The ATR cell was mounted within the sample compartment of a FTIR spectrometer (Bruker Vertex 70, RapidScan) and liquid streams were introduced at controlled flow rates using two high-pressure piston pumps (SSI Series 1), which were controlled using LabView™. Background scans were obtained at steady-state under pure flowing DI H_2O at 333 K after loading the ATR cell. Transient FTIR spectra showing changes upon introducing H_2O_2 were obtained while flowing aqueous H_2O_2 (0.03 M H_2O_2 in DI H_2O, 0.5 cm^3 min^{-1}) over the $Nb_{1.5}$-β coated IRE for 2.5 h at 333 K. Subsequently, a stream of pure DI H_2O was

pumped through the cell at 0.5 $cm^3\ min^{-1}$ for 1 h. Reported FTIR spectra for these experiments are the average of 1000 scans taken at a resolution of 4 cm^{-1} and were acquired every 66 s. Deconvolution of the steady-state FTIR spectrum was performed in OriginPro® by fixing the centers of the known framework vibrations attributed to the BEA framework of $Nb_{1.5}$-β (950 cm^{-1}, 1090 cm^{-1}) [43,46,47,56,57] and fitting the residual absorbance features with Gaussian functions.

Modulation excitation spectroscopy (MES) is a powerful technique, in which a periodic stimulation is applied to the system while acquiring spectra as a function of time. The time domain response is then converted to a phase domain response, and the spectral changes that occur at the frequency of the applied stimulation are extracted using a phase sensitive detection (PSD) method described by the following equation:

$$A_k(\varphi_k^{PSD}) = \frac{2}{T}\int_0^T A(t)\sin(k\omega t + \varphi_k^{PSD})dt, \quad (1)$$

where $A(t)$ and $A_k(\varphi_k^{PSD})$ are time- and phase-domain response of the active species respectively, T is the length of a time period, ω is the demodulation index and φ_k^{PSD} is the user defined phase demodulation angle. The application of the MES-PSD technique to FTIR spectra of intermediates on catalytic surfaces greatly increases the signal to noise ratio, suppresses the spectral contributions of static (i.e., spectator) species, and reveals high quality spectra containing contributions only of intermediates that change with respect to our applied stimulus (i.e., changing reactant concentrations) [58].

MES-PSD was used with ATR-IR to confirm that the predominant surface intermediates that form upon exposing $Nb_{1.5}$-β to aqueous H_2O_2 solutions (vide supra) are, in fact, active species for the epoxidation of olefins. MES-PSD experiments were performed by sinusoidally modulating the flow rates of two liquid streams (0.065 M H_2O_2 in CH_3CN, and 0.1 M C_6H_{10} in CH_3CN) from 0 to 0.5 $cm^3\ min^{-1}$ with a period of 0.5 h (which approximately corresponds to the turnover rate for epoxidation at these conditions), while maintaining a total flow rate of 0.5 $cm^3\ min^{-1}$. Spectra (128 scans, 4 cm^{-1}) were acquired every 8.5 s over 3 h. Flow rates were sinusoidally modulated and controlled on the two piston pumps through use of a LabView program that changes the set point of the pump in a stepwise manner every 0.5 s to approximate a sine wave with the desired frequency. Verification of sinusoidal reactant modulation was done by monitoring and absorbance feature at 1630 cm^{-1}, that is assigned to the ν_2 bending mode of H_2O [59], as a function of phase angle (Fig. S10) because H_2O was only present in the H_2O_2-containing stream. The recorded time domain spectra were resampled to a single period, and subsequently the spectra of the active species were extracted by PSD using Eq. (1). Details of the analysis method are described in Section S4.1.

3. Results and Discussion

3.1. Spectroscopic evidence for an irreversibly formed Nb-$(O_2)^-$ active intermediate

Metal-bound oxygen intermediates (i.e., superoxide (M-$(O_2)^-$), peroxide (M-$(O_2)^{2-}$), and hydroperoxide (M-OOH)), have been implicated in the epoxidation of olefins (e.g., propylene, cyclohexene, allylic alcohol) on metal-oxide catalysts (e.g., Ta-SBA-15 [21], TS-1 [60,61], and peroxoniobate ionic liquids [62]). The primary distinction between superoxide and peroxide species is the charge of the -O_2 moiety bound to the metal (i.e., superoxide (-O_2^-) and peroxide (-$(O_2)^{2-}$), and is, therefore, reflected in the oxidation state of the metal center (e.g., Ti^{III}-$(O_2)^-$ vs. Ti^{IV}-$(O_2)^{2-}$; or Nb^{IV}-$(O_2)^-$ vs. Nb^{V}-$(O_2)^{2-}$) [63,64]. Zecchina [65] and Frei [60] used combinations of IR, Raman, and UV-vis spectroscopy to show that reactive Ti^{IV}-$(O_2)^{2-}$ and/or Ti^{IV}-OOH species form by activation of H_2O_2 on TS-1. However, Ratnasamy et al. used in situ electron paramagnetic resonance (EPR) spectroscopy and determined that a paramagnetic Ti-superoxo (Ti^{III}-$(O_2)^-$) species is created on TS-1 upon activation of H_2O_2 and is active and selective for the epoxidation of allylic alcohol [66], and the exact identity of the reactive intermediate on TS-1 (specifically the Ti^{IV}-OOH or Ti^{III}-$(O_2)^-$) [63,64,67,68] is still debated. Similar types of hydroperoxo, peroxo, and superoxo species (i.e., Nb^{V}-OOH, Nb^{V}-$(O_2)^{2-}$, or Nb^{IV}-$(O_2)^-$) likely form when H_2O_2 reacts with Nb-β, and the vibrational structure, electronic transitions, and oxidation states, of the reactive complexes may be determined with the combination of FTIR, UV-vis, and X-ray photoelectron spectroscopy.

Fig. 3 shows FTIR spectra obtained upon exposing $Nb_{1.5}$-β to a flowing solution of H_2O_2 (0.03 M H_2O_2 in CH_3CN, 0.5 $cm^3\ min^{-1}$, 333 K). Fig. 3a shows that several new absorption features appear (i.e., 1040 cm^{-1}, 845 cm^{-1}, and 915 cm^{-1}), while existing absorption features attenuate (i.e., 950 cm^{-1}, 1090 cm^{-1}, and 1230 cm^{-1}) when $Nb_{1.5}$-β contacts H_2O_2, and Fig. 3b shows a representative steady-state FTIR spectrum acquired ~2 h after initiating the flow of H_2O_2. The steady-state spectrum (Fig. 3b) is comprised of seven individual components, which are listed in Table 2 along with the corresponding vibrational assignments. The negative absorbance features at 1090 and 1230 cm^{-1} and the positive feature at 915 cm^{-1} are attributed to the quenching and stimulation, respectively, of internal framework tetrahedral Si-O vibrational modes in the *BEA framework [46,47,56,57]. The absorbance feature at 750 cm^{-1} corresponds to the libration band of liquid-phase H_2O [59]. The absorbance peak observed at 845 cm^{-1} closely matches previously reported features at 837 cm^{-1} (Ti^{IV}-OOH/Ti^{IV}-$(O_2)^{2-}$ moieties on TS-1 [60,68]) and in the range of 850–888 cm^{-1} (Nb^{V}-OOH and Nb^{V}-$(O_2)^{2-}$) species on niobate ionic liquids [62] and bulk niobia [69], respectively. Consequently, we attribute this feature to Nb^{V}-OOH/Nb^{V}-$(O_2)^{2-}$ intermediate(s). The feature at 1040 cm^{-1} resembles that previously attributed to superoxide (O_2^-) moieties bound to Nb-centers of bulk Nb_2O_5 [69]. The formation of Nb^{V}-$(O_2)^{2-}$ and Nb^{IV}-$(O_2)^-$ species must occur concomitantly with the cleavage of an Nb-O-Si linkage shown by the formation of the negative feature at 950 cm^{-1} [43]. Additionally, Corma [70] and Wan [71] observed spectral features with similar wavenumber (900–1150 cm^{-1}) upon activating O_2 over CeO_2-based catalysts, which form superoxide species bound to differently coordinated metal cations (e.g., defect sites). Thus, the peak at 1040 cm^{-1} likely corresponds to an Nb^{IV}-$(O_2)^-$ (i.e., Nb-superoxide) intermediate. Finally, all of the spectral features (Table 2) persist when H_2O contacts the IRE (Fig. S11) after activation of H_2O_2 at 333 K, which shows that the Nb^{IV}-$(O_2)^-$ and Nb^{V}-OOH/Nb^{V}-$(O_2)^{2-}$ intermediates form irreversibly and do not spontaneously decompose in the presence of H_2O. This finding is also in agreement with results from DRUV-vis spectroscopy, discussed below, which are used to further identify and test the stability of these intermediates. The isomerization between hydroperoxide, peroxide, and superoxide intermediates has been proposed over TS-1 catalysts [65,67], which suggests that interconversion between Nb^{V}-OOH, Nb^{V}-$(O_2)^{2-}$, and Nb^{IV}-$(O_2)^-$ species may also occur upon the irreversible activation of H_2O_2 (Scheme 1). For the purpose of brevity, Nb^{IV}-$(O_2)^-$ will be referred to as Nb^{IV}-(O_2) while Nb^{V}-OOH and Nb^{V}-$(O_2)^{2-}$ will be collectively referred to as Nb^{V}-(O_2).

X-ray photoelectron spectroscopy (XPS) was used to determine the oxidation state of Nb in both untreated and H_2O_2-activated (Section 2.4) $Nb_{5.0}$-β samples in order to verify the presence of Nb^{IV} species (i.e., Nb^{IV}-(O_2)). Fig. 4a shows the XPS spectra for untreated $Nb_{5.0}$-β in the Nb 3d region (200–220 eV), which possesses a doublet with absorbance peaks centered at 210.6 and 208.0 eV that

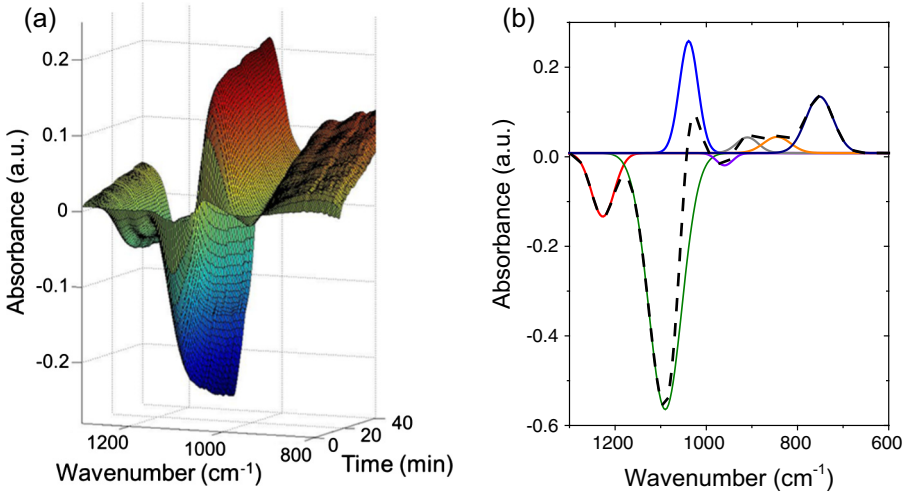

Fig. 3. In situ FTIR spectra obtained upon exposing $Nb_{1.5}$-β to H_2O_2 (0.03 M H_2O_2 in CH_3CN, 0.5 cm^3 min^{-1}, 333 K) showing, (a) changes in the infrared spectra of Nb-β upon first contact with flowing H_2O_2, and (b) deconvoluted FTIR spectrum obtained at steady-state after flowing H_2O_2 for 2 h. Vibrational frequencies and peak assignments are given in Table 2.

Table 2
Observed vibrational frequencies and mode assignments for the deconvoluted FTIR spectrum in Fig. 3b.

Vibrational frequency (cm^{-1})	Vibrational assignment	Parent species
750	Libration [59]	Water
845	ν(O—O) [67,69]	Nb^{V}-OOH/ Nb^{V}-$(O_2)^{2-}$
915	Internal tetrahedral – asymmetric stretch [46]	*BEA Framework
950	ν(Si—O—Nb) [43,47]	Nb-β
1040	ν(O—O) [69–71]	Nb^{IV}-$(O_2)^{-}$
1090	Internal tetrahedral – asymmetric stretch [46,47,56,57]	*BEA Framework
1230	Internal tetrahedral – asymmetric stretch [46,47,56,57]	*BEA Framework

correspond to Nb^{V} $3d_{3/2}$ and $3d_{5/2}$, respectively [72,73] (fitting that demonstrates the absence of Nb^{IV} is provided in the SI, Fig. S7). These features shift to lower binding energies when the $Nb_{5.0}$-β sample has been treated with H_2O_2 (details given in Section 2.4). Fig. 4b shows that XPS spectra of H_2O_2-activated $Nb_{5.0}$-β contains overlapping doublet features with doublets at 210.6 and 208.0 eV as well as at 209.7 and 207.0 eV, which resemble reported values for Nb^{V} and Nb^{IV-} species [72,73], and is consistent with the presence of the proposed Nb^{V}-(O_2) and Nb^{IV}-(O_2) species, respectively. Under ultra-high vacuum conditions (i.e., 10^{-9} Torr), the preferred state of the H_2O_2-activated Nb-β is Nb^{IV}-(O_2), because the lack of free protons favors the formation of the superoxo species, as shown for H_2O_2-activated TS-1 [66], which explains why the magnitude of the features for Nb^{IV} is much larger than for Nb^{V} on H_2O_2-treated materials.

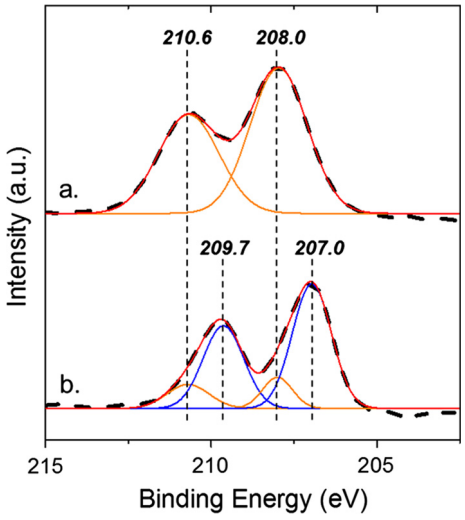

Fig. 4. X-ray photoelectron spectra (black, dashed) of the Nb 3d region with peak fittings (colored, solid) for (a) untreated $Nb_{5.0}$-β and (b) H_2O_2-treated $Nb_{5.0}$-β. The peak fittings from the different oxidation states are color-coded for clarity: Nb^{IV} (blue, –), Nb^{V} (orange, –), and cumulative peak fit (red, –). Spectra are referenced to an aliphatic C 1 s feature at 284.8 eV. The H_2O_2 treatment procedure is described in Section 2.4.

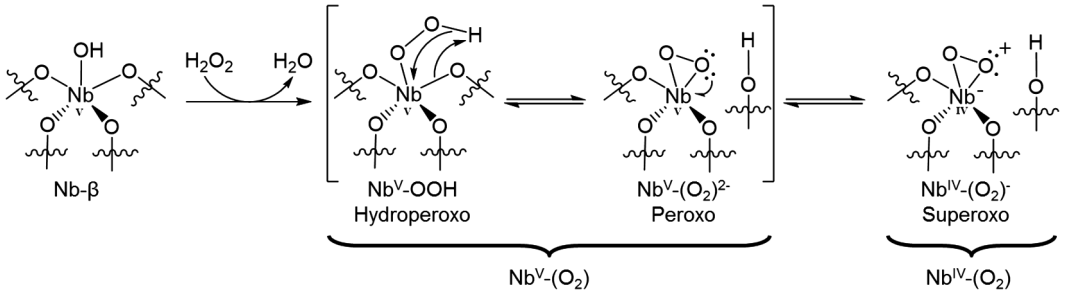

Scheme 1. Activation of H_2O_2 to form Nb^{V}-OOH with the interconversion of Nb^{V}-OOH, Nb^{V}-$(O_2)^{2-}$, and Nb^{IV}-$(O_2)^{-}$. The oxidation state of each Nb center is depicted beneath the atom.

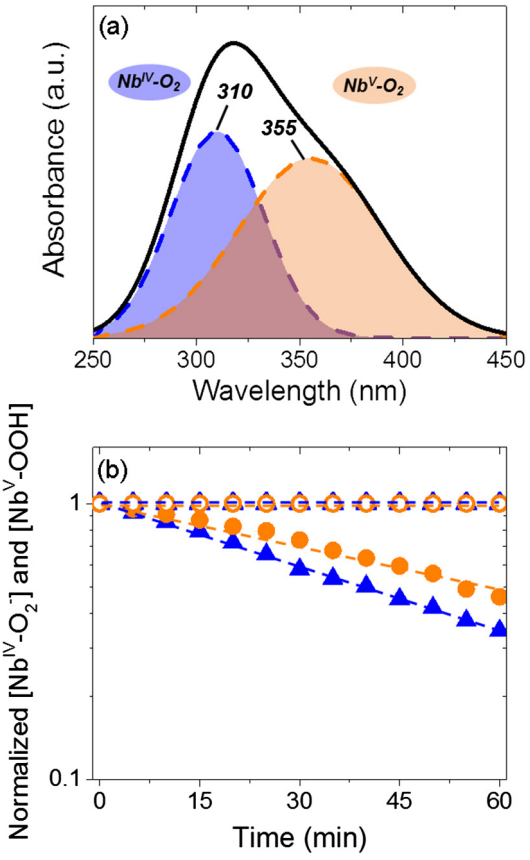

Fig. 5. (a) UV-vis spectra of H_2O_2-treated $Nb_{0.3}$-β in flowing CH_3CN (0.4 M H_2O) at 348 K (–, black), and deconvoluted peaks (dashed) centered at 301 (–, blue) and 365 nm (–, orange); and (b) changes in the normalized coverages of [Nb^{IV}-(O_2)] (330 nm, ▲) and [Nb^{V}-(O_2)] (370 nm, ●) as a function of time after contact with C_6H_{10} in CH_3CN (0.1 M C_6H_{10}, 0.4 M H_2O, 1 cm^3 min^{-1}, closed symbols) or pure DI H_2O (1 cm^3 min^{-1}, open symbols) at 313 K. Dashed lines are intended to guide the eye.

The surface intermediates (i.e., Nb^{IV}-(O_2) and Nb^{V}-(O_2)) generated by reacting $Nb_{0.3}$-β with H_2O_2 appear as distinct absorption features in in situ DRUV-vis spectroscopy. Fig. 5a shows a UV-vis spectrum of H_2O_2-treated $Nb_{0.3}$-β (Section 2.5), which contains two distinct absorbance bands at 310 and 355 nm that are assigned to Nb^{IV}-(O_2) and Nb^{V}-(O_2) moieties, respectively [67,69]. Fig. 5b shows that the normalized intensities of the Nb^{IV}-(O_2) (310 nm) and Nb^{V}-(O_2) (355 nm) features decrease with an exponential dependence on time when the H_2O_2-treated $Nb_{0.3}$-β contacts a flowing solution of C_6H_{10} in CH_3CN (0.1 M C_6H_{10}, 0.4 M H_2O, 1 cm^3 min^{-1}). However, Fig. 5b shows also that neither the 310 or the 355 nm absorbance feature changes noticeably even after one hr of contact with a flowing stream of pure DI H_2O (1 cm^3 min^{-1}), which demonstrates further that these intermediates (i.e., Nb^{IV}-(O_2) or Nb^{V}-(O_2)) form irreversibly. These data, along with steady-state IR spectra obtained under a flow of H_2O (Fig. S11), strongly suggest that Nb-β activates H_2O_2 irreversibly to form both Nb^{IV}-(O_2) and Nb^{V}-(O_2) intermediates, in contrast to proposed mechanisms on similar Ti- and Ta-based catalysts, where H_2O_2 activation is proposed to occur reversibly (and often in a quasi-equilibrated fashion) [21–23,39].

The intensities of these two UV-vis features (Fig. 5a, 310 and 355 nm, normalized by their initial intensities) attenuate with an exponential dependence on time at different rates when H_2O_2-treated $Nb_{0.3}$-β contacts a solution of C_6H_{10} in CH_3CN (0.1 M C_6H_{10}, 0.4 M H_2O, 1 cm^3 min^{-1}), and the differences in the rates of consumption of these species reflect the nature of the elementary steps that consume Nb^{IV}-(O_2) and Nb^{V}-(O_2) (Scheme 2). Nb^{IV}-(O_2) and Nb^{V}-(O_2) species may be consumed by reaction with C_6H_{10}, but these species may also interconvert during the course of the reaction, as shown in Schemes 1 and 2 [65]. Consequently, the change in coverage of Nb^{IV}-(O_2) and Nb^{V}-(O_2) depends on the summed rates of formation and consumption of each species, which take the forms of the following:

$$\frac{d[Nb^{IV}-(O_2)]}{dt} = k_a[Nb^{V}-(O_2)] - k_b[Nb^{IV}-(O_2)] - k_d[Nb^{IV}-(O_2)][C_6H_{10}] \quad (2)$$

$$\frac{d[Nb^{V}-(O_2)]}{dt} = k_b[Nb^{IV}-(O_2)] - k_a[Nb^{V}-(O_2)] - k_c[Nb^{V}-(O_2)][C_6H_{10}] \quad (3)$$

where [Nb^{IV}-$(O_2)^-$] and [Nb^{V}-(O_2)] represent the coverage of Nb^{IV}-(O_2) and Nb^{V}-(O_2), [C_6H_{10}] is the concentration of C_6H_{10}, k_a is the rate constant for the interconversion of Nb^{V}-(O_2) to Nb^{IV}-(O_2), k_b is the rate constant for the interconversion of Nb^{IV}-(O_2) to Nb^{V}-(O_2), and k_c and k_d are the rate constants for the epoxidation of C_6H_{10} with Nb^{V}-(O_2) and Nb^{IV}-(O_2), respectively. Pseudo first-order kinetics are assumed for the reaction of Nb^{V}-(O_2) and Nb^{IV}-(O_2) with C_6H_{10}, and [C_6H_{10}] is constant because C_6H_{10} flows continuously through the reactor and conversion of C_6H_{10} is negligible. MATLAB™ is used to numerically solve these two coupled differential equations (Eqs. (2) and (3)), while iteratively optimizing the rate constants (i.e., k_i) to fit the experimental data (Section S3.2), and Table 3 shows the optimized rate constants for Scheme 2. The value of k_d is calculated to be $\sim 2 \cdot 10^4$ times that of k_c, which shows directly that Nb^{IV}-(O_2) is the reactive species that is responsible for all observed epoxidation rates and that this species is more than four orders of magnitude more reactive than the Nb^{V}-(O_2) species. The consumption of Nb^{V}-(O_2) is, therefore, attributed to its interconversion to reform additional Nb^{IV}-(O_2) throughout the course of the reaction (i.e., value of k_b significantly greater than k_a). Collectively, these data show that both Nb^{IV}-(O_2) and Nb^{V}-(O_2) are formed upon activation of H_2O_2, but only Nb^{IV}-(O_2) participates directly in the epoxidation of C_6H_{10}, while Nb^{V}-(O_2) simply interconverts to partially replenish Nb^{IV}-(O_2) during reaction.

Modulation excitation spectroscopy (MES) experiments were employed to support the conclusion that Nb^{IV}-(O_2) is the active intermediate for the epoxidation of C_6H_{10}. The flow rates H_2O_2 and cyclohexene in CH_3CN (Section 2.5) were modulated sinusoidally with the intent to periodically populate the catalyst surface with the active species (i.e., Nb^{IV}-(O_2) and Nb^{V}-(O_2)) and subsequently consume these species by cyclohexene epoxidation. Fig. 6a displays phase domain spectra (obtained by resampling all spectra into a single period, converting to the phase domain, and employing phase sensitive detection, see Section S4.1), that show only the active surface species whose coverages change at frequencies comparable to the modulation (i.e., contributions from spectator species are suppressed). Fig. 6 shows a broad feature at 864 cm^{-1} that is assigned to ν(C—C) of a C_6 ring of either C_6H_{10} or $C_6H_{10}O$ [74]. Notably, this broad 864 cm^{-1} feature is perfectly out of phase (i.e., 180° phase shift) with the absorbance feature corresponding to the active Nb^{IV}-(O_2) intermediate (1024 cm^{-1}, Fig. 6b), which supports the conclusion that Nb^{IV}-(O_2) species are consumed by reaction with C_6H_{10}, which is followed by the replacement of Nb^{IV}-(O_2) with C_6H_{10} or $C_6H_{10}O$ as the MARI on the catalyst surface. Unfortunately, the spectroscopic feature at 845 cm^{-1} attributed to Nb^{V}-(O_2) (Fig. 3b, Nb^{V}-(O_2)) is overwhelmed by the broad feature at 864 cm^{-1}, which precludes clear analysis of how the coverage of Nb^{V}-(O_2) species varies with the changes in the concentrations of C_6H_{10} and H_2O_2. However, the previous analysis of the in situ UV-vis spectra (Fig. 5, Table 3)

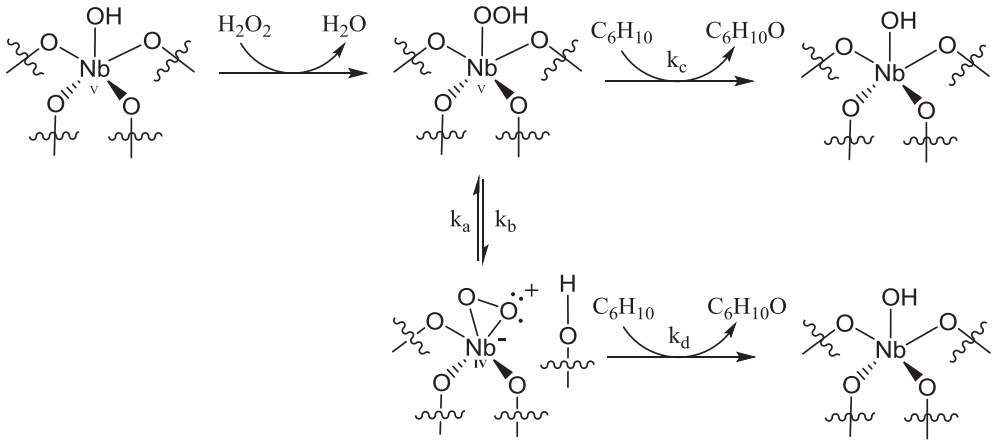

Scheme 2. Formation and consumption of active species on Nb-β. Nb^{V}-(O_2) (Nb^{IV}-OOH shown) and Nb^{IV}-(O_2) form upon reaction of H_2O_2 with Nb-β, and these species interconvert, and may be consumed by reaction with C_6H_{10}. [a]Formation of Nb^{V}-(O_2) and Nb^{IV}-(O_2) occurs during the activation of H_2O_2 over $Nb_{0.3}$-β by flow of H_2O_2 in CH_3CN (Section 2.5).

Table 3
Numerically optimized rate constants k_i for the interconversion of Nb^{V}-(O_2) and Nb^{IV}-(O_2) and reaction with C_6H_{10} (Scheme 2). See Section S3.2 for a complete description of the procedure used to optimize parameters and fit the experimental data.

k_i	Numerically optimized value (min^{-1})
k_a	$2.3 \cdot 10^{-4}$
k_b	$2.0 \cdot 10^{-2}$
k_c	$1.3 \cdot 10^{-5}$
k_d	$2.7 \cdot 10^{-1}$

shows already that the Nb^{V}-(O_2) intermediates do not directly participate in epoxidation reactions. In summary, the combined in situ FTIR and UV-vis data (Figs. 3, 5–6) suggest that H_2O_2-activation over $Nb_{1.5}$-β occurs irreversibly and that Nb^{IV}-(O_2) (and not Nb^{V}-(O_2)) is the active intermediate for C_6H_{10} epoxidation upon activation of H_2O_2 by Nb-β.

The conclusion that Nb^{IV}-(O_2) is the active species for olefin epoxidation is not immediately intuitive, because superoxide species are typically thought to be one electron oxidants (or even reductants) and not two-electron ($2e^-$) oxidants. In order for Nb-(O_2) to undergo a $2e^-$ oxidation (e.g., olefin epoxidation), the process must involve concomitant oxidation of the Nb-metal center from Nb^{IV} to Nb^{V} and the reformation of a Nb-O-Si framework bond. Similar processes have been proposed to occur through a biradical, stepwise reaction on homogeneous vanadium complexes [75,76], and Nb-$(O_2)^-$ superoxide species may react in an analogous manner (Scheme S2). The epoxidation of cis-stilbene provides one method to test this hypothesis and to determine whether the epoxidation reaction proceeds through a concerted reaction or by a stepwise reaction, which would be consistent with the participation of Nb^{IV}-(O_2) as the active intermediate [77]. The reaction of cis-stilbene with $Nb_{1.5}$-β (0.01 M cis-stilbene, 0.01 M H_2O_2, in CH_3CN, 323 K) produces nearly equimolar quantities of cis- and trans-stilbene oxides (the exact ratio of cis- to trans-stilbene oxide is equal to 0.96). This equimolar ratio suggests that olefin epoxidation over Nb-β occurs through the biradical stepwise mechanism (e.g., Scheme S2), which provides sufficient time for the coordinated olefin intermediate to isomerize about the central C=C bond prior to oxirane cyclization. Collectively, these spectroscopic data and product selectivities provide compelling evidence that H_2O_2 irreversibly activates over Nb-β to form a pool of Nb^{V}-(O_2) and Nb^{IV}-(O_2) species that interconvert, and that from this pool, Nb^{IV}-(O_2) species participate directly in the epoxidation of olefins by a biradical, stepwise reaction pathway (Scheme S2).

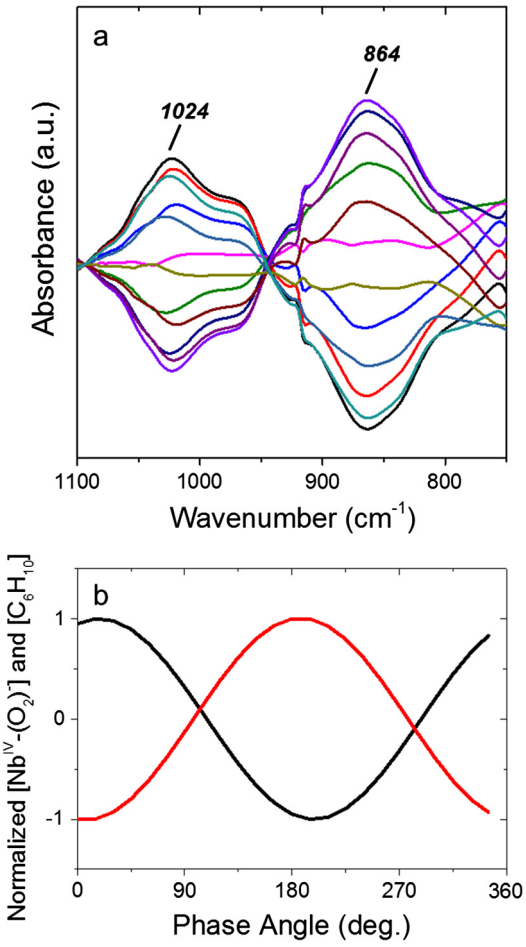

Fig. 6. (a) Phase-angle resolved in situ FTIR spectra showing spectral contributions of active surface species for C_6H_{10} epoxidation on $Nb_{1.5}$-β, and (b) Normalized Nb^{IV}-$(O_2)^-$ (1024 cm^{-1}, black, -) and C_6H_{10} (864 cm^{-1}, red, -) IR-feature absorbances as a function of phase angle. Spectra were obtained while sinusoidally modulating the flow rates of C_6H_{10} (0.1 M C_6H_{10} in CH_3CN) and H_2O_2 (0.065 H_2O_2 in CH_3CN) solutions (0.5 cm^3 total volumetric flow rate, 333 K, Section 2.5). Lines correspond to FTIR spectra obtained at 30° increments of the demodulation phase angle.

3.2. Dependence of turnover rates on reactant concentrations and mechanistic interpretation

Fig. 7a shows turnover rates for the formation of $C_6H_{10}O$ as a function of [C_6H_{10}] (0.01–5 M C_6H_{10}, 1 mM H_2O_2, 313 K) over

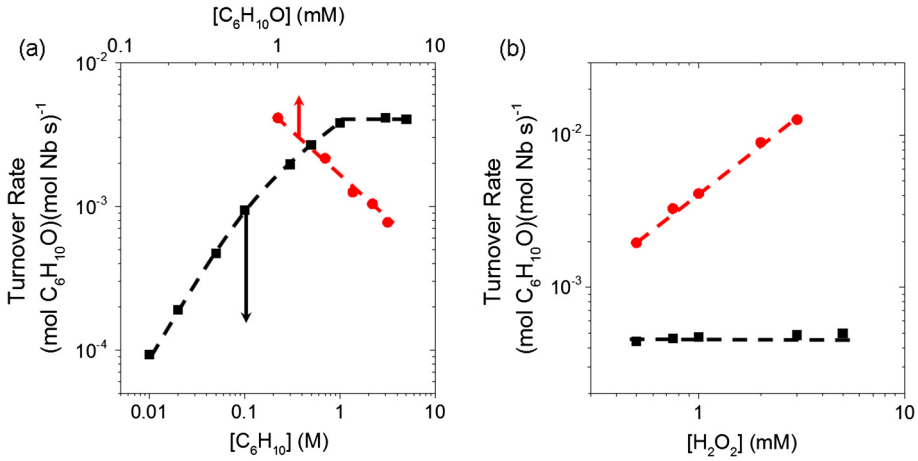

Fig. 7. Turnover rates for the formation of $C_6H_{10}O$ as a function of (a) $[C_6H_{10}]$ (■, 1 mM H_2O_2, $Nb_{1.5}$-β, 313 K) and $[C_6H_{10}O]$ (●, 3 M C_6H_{10}, 1 mM H_2O_2, $Nb_{1.5}$-β, balance CH_3CN to 30 cm^3, 313 K) and (b) as a function of $[H_2O_2]$ (50 mM C_6H_{10} (■) or 3 M C_6H_{10} (●), $Nb_{1.5}$-β, 313 K). Error bars omitted for clarity, and lines are intended to guide the eye.

$Nb_{1.5}$-β, and Fig. 7b shows turnover rates for $C_6H_{10}O$ formation as a function of $[H_2O_2]$ (0.5–5 mM H_2O_2, 0.05 and 3 M C_6H_{10}, 313 K). Rates of epoxidation depend linearly on $[C_6H_{10}]$ and do not change with $[H_2O_2]$ (0.5–5 mM, 5 mM C_6H_{10}) at low $[C_6H_{10}]$ (0.01–0.1 M C_6H_{10}), which suggests that the active sites are saturated with an H_2O_2-derived intermediate, such as adsorbed H_2O_2 or Nb^{IV}-(O_2)/Nb^{V}-(O_2) (Section 3.1). Rates of epoxidation become independent of $[C_6H_{10}]$ as $[C_6H_{10}]$ increases further (0.1–5 M C_6H_{10}), and this change indicates that the identity of the MARI changes to a C_6H_{10}-derived intermediate (e.g., C_6H_{10} or $C_6H_{10}O$). This is likely due to the increasing amount of C_6H_{10}-derived species (i.e., C_6H_{10} or $C_6H_{10}O$) occupying additional Nb active sites which decreases the number of sites that exist as the active Nb^{IV}-$(O_2)^-$ species. Additionally, Fig. 7b shows the turnover rates become proportional to $[H_2O_2]$ (0.5–3 mM) at higher $[C_6H_{10}]$ (3 M), which is consistent with a change in the MARI from an H_2O_2-derived intermediate to a C_6H_{10}-derived MARI. Fig. 7a shows that the rate of epoxidation depends inversely on the $C_6H_{10}O$ concentration (1–5 mM) within this same range of $[C_6H_{10}]$ (3 M) and $[H_2O_2]$ (1 mM), which implies that $C_6H_{10}O$ binds strongly to the active site and inhibits rates.

Previously proposed mechanisms for olefin epoxidation on metal-oxide catalysts (i.e., TS-1 [39] and Ta-SBA-15 [21,22]) assume that steps for the adsorption of the olefin, H_2O_2, epoxide, and the formation of the reactive intermediate (e.g., M-OOH or

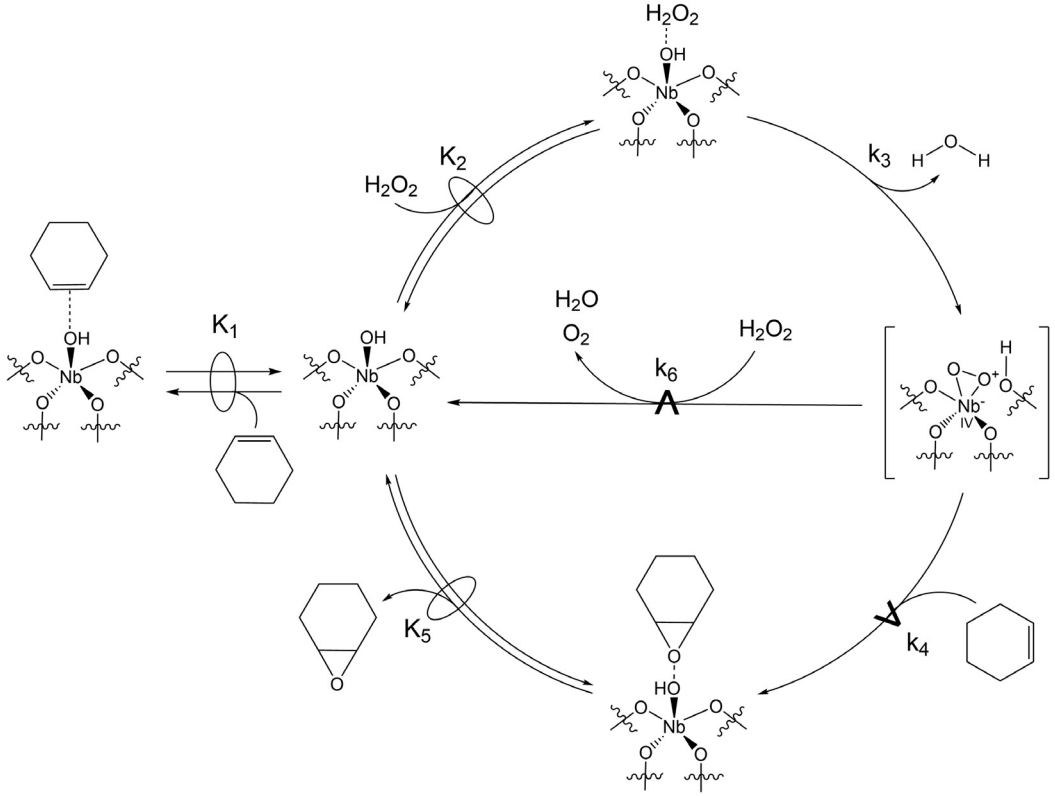

Scheme 3. Proposed mechanism for cyclohexene epoxidation with H_2O_2 over Nb-β. Subscripts for rate constants or equilibrium constants (k_x or K_x, respectively) denote the number of the elementary step. The proposal for an active Nb^{IV}-(O_2) intermediate is supported by XPS (Fig. 4) and time-resolved in situ FTIR (Figs. 3 and 6) and UV-vis spectroscopy (Fig. 5).

M-$(O_2)^-$) are quasi-equilibrated (QE) and that the epoxidation of the olefin by the M-(O_2) species is the sole kinetically relevant (KR) step. Such mechanisms give rate expressions (Section S5 contains the rate expressions based on these previous models) that predict epoxide formation rates that do not depend on $[H_2O_2]$ and increase linearly with $[C_6H_{10}]$ at low $[C_6H_{10}]$ (Eq. S5.6), and that reaction rates become constant with $[C_6H_{10}]$ but proportional to $[H_2O_2]$ at greater $[C_6H_{10}]$ (Eq. S5.7). The previously described mechanisms and rate expressions for cyclohexene and cyclooctene epoxidation on TS-1 [39] and Ta-SiO_2 [21,22] are consistent with the rate data shown here (Fig. 7a and b) as a function of $[H_2O_2]$ and $[C_6H_{10}]$, but fail to predict the dependence on $[C_6H_{10}O]$. These previous studies did not report changes in rates as a function of the epoxide concentration. Several aspects of the previously proposed mechanisms are inconsistent with the results shown in this article (and perhaps with chemical intuition). The in situ FTIR and UV-vis spectra show that neither the Nb^{IV}-(O_2) nor the Nb^{V}-(O_2) species decompose or reform H_2O_2 in the presence of H_2O (Section 3.1), which demonstrate that these intermediates form irreversibly (Scheme 3, step 3) when H_2O_2 reacts with the metal center (e.g., Nb). Notably, these results disagree with previous assumptions that M-(O_2) species form on Ti- and Ta-based catalysts by QE processes [21,22,39]. Chemical intuition also suggests that H_2O_2 is not likely to reform from the Nb^{IV}-(O_2) and Si-OH groups (created by hydroperoxidolysis of the Nb-O bond) when the sample is hydrated (Scheme 3, reverse step 3), because the formation of H_2O_2 from H_2O and the surface function is most likely endothermic and thermodynamically disfavored under these conditions. Therefore, the mechanism shown below (Scheme 3) differs from previous proposals in a few significant ways.

Scheme 3 depicts our proposed mechanism for the epoxidation of C_6H_{10} with H_2O_2 over Nb-β. This scheme includes quasi-equilibrated adsorption and desorption of C_6H_{10} (step 1), H_2O_2 (step 2), and $C_6H_{10}O$ (step 5), and the irreversible formation of Nb^{IV}-(O_2) (step 3). The epoxidation of C_6H_{10} (step 4) and the bimolecular decomposition of H_2O_2 (step 6) occur in kinetically relevant, irreversible steps that involve Nb^{IV}-(O_2) and C_6H_{10} or H_2O_2 co-reactants, respectively. A Langmuir-Hinshelwood mechanism seems unlikely because the average distance between adjacent Nb atoms (2.64 nm [78]) is too large for interaction between adsorbates [79,80]. Scheme 3 suggests net $C_6H_{10}O$ formation rates (r_E) that depend on the number of Nb^{IV}-(O_2) intermediates and the concentration of C_6H_{10} in solution as follows:

$$r_E = k_4[C_6H_{10}] \cdot [Nb^{IV} - (O_2)] \quad (4)$$

where $[Nb^{IV}$-$(O_2)]$ is the number of Nb^{IV}-(O_2) species and k_4 is the rate constant for the epoxidation of C_6H_{10} with Nb^{IV}-(O_2). Application of the pseudo-steady state hypothesis (PSSH) to the number of Nb^{IV}-(O_2) complexes yields the following rate expression:

$$\frac{r_E}{[L]} = \frac{k_3k_4K_2[C_6H_{10}] \cdot [H_2O_2] \cdot [*]}{(k_4[C_6H_{10}] + k_6[H_2O_2])} \quad (5)$$

where k_x and K_x are the rate and equilibrium constants, respectively, for each step x (Scheme 3) and [*] is the number of available Nb-OH moieties (i.e., active sites) that can bind and react with species in solution (or weakly associate with silica near the active site). An expression for

$[*]$

is given from the sum of all likely surface intermediates:

$$[L] = ([*] + [C_6H_{10}^*] + [H_2O_2^*] + [Nb - (O_2)] + [C_6H_{10}O^*]) \quad (6)$$

where $[L]$ is the total number of active sites, $[Nb$-$(O_2)]$ is the pool of Nb^{IV}-(O_2) and Nb^{V}-(O_2) species, and $[C_6H_{10}^*]$, $[H_2O_2^*]$, and $[C_6H_{10}O^*]$ are the number of adsorbed C_6H_{10}, H_2O_2, and $C_6H_{10}O$ species, respectively. Eq. (6) can then be re-stated in terms of the rate and equilibrium constants as well as the liquid-phase reactant concentrations by application of the PSSH to each specie:

$$[L] = \left([*] + K_1[C_6H_{10}] \cdot [*] + K_2[H_2O_2] \cdot [*] + \frac{k_3K_2[H_2O_2] \cdot [*]}{(k_4[C_6H_{10}] + k_6[H_2O_2])} + K_5[C_6H_{10}O] \cdot [*]\right) \quad (7)$$

The combination of Eqs. (5) and (7) yields a complete rate expression for $C_6H_{10}O$ formation:

$$\frac{r_E}{[L]} = \frac{k_3k_4K_2[C_6H_{10}] \cdot [H_2O_2]}{(k_4[C_6H_{10}] + k_6[H_2O_2])\left(1 + K_1[C_6H_{10}] + K_2[H_2O_2] + \frac{k_3K_2[H_2O_2]}{(k_4[C_6H_{10}] + k_6[H_2O_2])} + K_5[C_6H_{10}O]\right)} \quad (8)$$

The form of this full rate equation simplifies in the limit when active sites become saturated with H_2O_2-derived intermediates (i.e., Nb^{IV}-(O_2)/Nb^{V}-(O_2) are the MARI) as is expected in the limit of low $[C_6H_{10}]$:$[H_2O_2]$ reactant ratios:

$$\frac{r_E}{[L]} = k_4[C_6H_{10}] \quad (9)$$

Eq. (9) is consistent with the $C_6H_{10}O$ formation rates that increase in proportion to $[C_6H_{10}]$ at low $[C_6H_{10}]$ (Fig. 7a, 0.01–0.1 M C_6H_{10}), and which do not depend on $[H_2O_2]$ (Fig. 8b, 0.5–5 mM H_2O_2, 5 mM C_6H_{10}). Turnover rates for epoxidation depend inversely on $[C_6H_{10}O]$ at high $[C_6H_{10}]$, because adsorbed $C_6H_{10}O$ becomes the MARI at values of $[C_6H_{10}]$ greater than 0.5 M. Intuitively, $C_6H_{10}O$ becomes the MARI at high $[C_6H_{10}]$ only when small amounts of epoxide (present as a reagent contaminant, or upon initial formation of $C_6H_{10}O$) are present. In this limit, Eq. (8) simplifies to the following:

$$\frac{r_E}{[L]} = \frac{k_3k_4K_2[C_6H_{10}][H_2O_2]}{(k_4[C_6H_{10}] + k_6[H_2O_2])[C_6H_{10}O]} \quad (10)$$

The denominator in Eq. (10) shows that the rate of epoxidation when adsorbed $C_6H_{10}O$ is the MARI depends on the propensity of Nb-$(O_2)^-$ to epoxidize C_6H_{10} ($k_4[C_6H_{10}]$) relative to decompose by reaction with H_2O_2 ($k_6[H_2O_2]$).

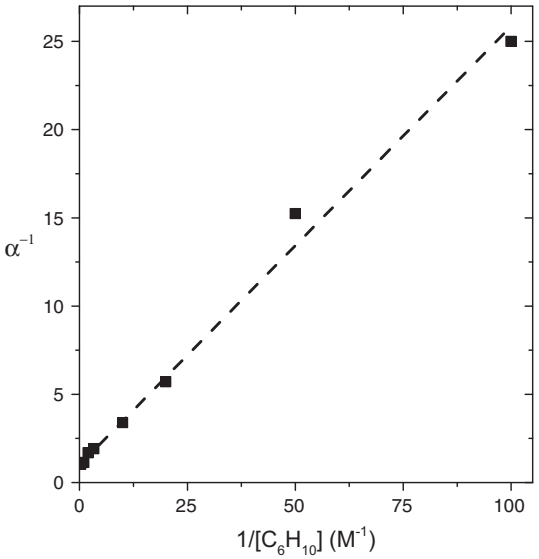

Fig. 8. Ratio of total H_2O_2 consumption to $C_6H_{10}O$ formation as a function of inverse C_6H_{10} concentration on $Nb_{1.5}$-β (1 mM H_2O_2, 313 K). Dashed line represents linear fit to Eq. (15) with an r^2 of 0.995.

3.3. Mechanistic interpretation for H_2O_2 decomposition over Nb-β

Control experiments show that in the absence of Nb-β, no H_2O_2 decomposition is observed after 4 h at 333 K (data not shown). Values of $[H_2O_2]$, however, decrease steadily with time when H_2O_2 contacts Nb-β. The unimolecular decomposition of H_2O_2 via a Nb^{IV}-(O_2) intermediate cannot account for H_2O_2 consumption, because FTIR (Fig. S11) and UV-vis spectra (Fig. 5b) show that the Nb^{IV}-(O_2) species are stable over multiple hours when they are isolated from liquid-phase C_6H_{10} and H_2O_2. Therefore, H_2O_2 decomposition likely occurs through a bimolecular reaction between Nb^{IV}-(O_2) and a liquid-phase H_2O_2 molecule [22]. The rate of this reaction follows the form:

$$r_D = k_6[H_2O_2]\cdot[Nb^{IV}-(O_2)] \tag{11}$$

where r_D is the rate of H_2O_2 consumption via decomposition over Nb-β and k_6 is the rate constant for the bimolecular reaction between Nb^{IV}-(O_2) and a H_2O_2 molecule in solution. The expression for total H_2O_2 consumption is obtained from the sum of Eqs. (4) and (11) to yield the following:

$$r_{H_2O_2} = k_4[C_6H_{10}]\cdot[Nb^{IV}-(O_2)] + k_6[H_2O_2]\cdot[Nb^{IV}-(O_2)] \tag{12}$$

where $r_{H_2O_2}$ is the rate of total H_2O_2 consumption through epoxidation and decomposition processes. Application of the PSSH to Nb^{IV}-(O_2) (Section 3.2, algebraic manipulation omitted) allows Eq. (12) to be restated in terms of liquid concentrations as follows:

$$\frac{r_{H_2O_2}}{[L]} = \frac{k_3K_2[H_2O_2]}{\left(1+K_1[C_6H_{10}]+K_2[H_2O_2]+\frac{k_3K_2[H_2O_2]}{(k_4[C_6H_{10}]+k_6[H_2O_2])}+K_5[C_6H_{10}O]\right)} \tag{13}$$

Eq. (13) shows that the rate of H_2O_2 consumption depends only on the rate of C_6H_{10} epoxidation ($k_4[C_6H_{10}]$) or H_2O_2 decomposition ($k_6[H_2O_2]$) when surfaces are saturated with Nb^{IV}-(O_2). For all other identities of the MARI, H_2O_2 consumption is controlled by the rate of H_2O_2 activation at the reactive Nb-centers. This shows that the H_2O_2 selectivity for epoxidation can be controlled by reaction at conditions which solely maximize the turnover rate for $C_6H_{10}O$ formation.

3.4. H_2O_2 selectivity for epoxidation and mechanistic implications

The selective use of H_2O_2 for epoxidations is a necessary economic consideration before a catalyst can be adapted for industrial epoxidation chemistries, and consequently requires the ratio of the rates for epoxidation to H_2O_2 consumption (i.e., $r_E/r_{H_2O_2}$) to approach unity (i.e., 100% selectivity). From the combination of Eqs. (8) and (13), the ratio of the rate of $C_6H_{10}O$ formation to that for H_2O_2 consumption (Fig. S12) yields the following expression:

$$\alpha = \frac{r_E}{r_{H_2O_2}} = \frac{k_4[C_6H_{10}]}{k_4[C_6H_{10}]+k_6[H_2O_2]} \tag{14}$$

Eq. (14) may be linearized, with respect to inverse $[C_6H_{10}]$, by taking the inverse of α to give the following:

$$\alpha^{-1} = \frac{r_{H_2O_2}}{r_E} = 1+\frac{k_6[H_2O_2]}{k_4[C_6H_{10}]} \tag{15}$$

Fig. 8 shows values of α^{-1} as a function of inverse $[C_6H_{10}]$ (1 mM $[H_2O_2]$, 313 K). The value of the slope (found to be 0.25) shows that $k_4[C_6H_{10}] \gg k_6[H_2O_2]$ at high $[C_6H_{10}]$ (1–5 M), which indicates that in the limit of high $[C_6H_{10}]$:$[H_2O_2]$, Eq. (10) can be approximated as follows:

$$\frac{r_E}{[L]} = \frac{k_3K_2[H_2O_2]}{[C_6H_{10}O]} \tag{16}$$

which qualitatively agrees with the trends observed in Fig. 7a (i.e., $r_E \sim[C_6H_{10}]^0\cdot[C_6H_{10}O]^{-1}$) and 7b ($r_E \sim[H_2O_2]^1$) when $[C_6H_{10}]$:$[H_2O_2]$ reactant ratios are large. Overall, the proposed mechanism (Scheme 3) agrees with the spectroscopic observations in Figs. 3–6 and the rate data presented in Figs. 7 and 8.

3.5. Epoxidation and decomposition activation enthalpies ($\Delta H^{\ddagger}$) and entropies ($\Delta S^{\ddagger}$)

Transition-state theory (TST) provides a theoretical foundation to relate the stability of a reference state (e.g., the most abundant reactive intermediate) to an activated complex that facilitates the reaction (i.e., the transition state) [4,81]. Here, the values of apparent activation enthalpies ($\Delta H^{\ddagger}$) and entropies ($\Delta S^{\ddagger}$) can be used to compare the relative stability of the transition states that selectively activate H_2O_2 and epoxidize an olefin to those that facilitate non-selective H_2O_2 decomposition. TST, in conjunction with our proposed mechanism (Scheme 3), proposes that the reactant species (e.g., Nb^{IV}-(O_2) and C_6H_{10}) exist in equilibrium with the transition state (i.e., Nb^{IV}-(O_2)-$C_6H_{10}^{\ddagger}$) for the elementary step for epoxidation (Scheme 4) [54].

The combined equilibria are expressed as follows:

$$Nb^{IV}-(O_2)+C_6H_{10} \overset{K^{\ddagger}_E}{\rightleftharpoons} \left[Nb-(O_2)-C_6H_{10}^{\ddagger}\right] \tag{17}$$

$$Nb^{IV}-(O_2)+H_2O_2 \overset{K^{\ddagger}_D}{\rightleftharpoons} \left[Nb-(O_2)-H_2O_2^{\ddagger}\right] \tag{18}$$

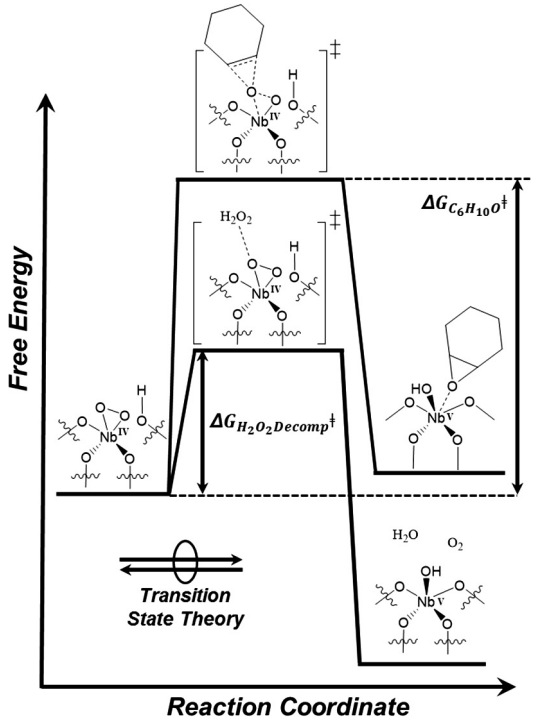

Scheme 4. Thermochemical cycle depicting changes in free energy in the reaction sequence shown in Scheme 3, which forms transition states for epoxide formation and H_2O_2 decomposition through reaction with Nb^{IV}-(O_2).

Table 4
Catalyst activation enthalpies and entropies for C_6H_{10} epoxidation and H_2O_2 decomposition on a Nb^{IV}-(O_2)/Nb^{V}-(O_2) covered surface.[a]

Catalyst	$\Delta H_E^{\ddagger}$ (kJ mol^{-1})	$\Delta S_E^{\ddagger}$ (J mol^{-1} K^{-1})	$\Delta H_D^{\ddagger}$ (kJ mol^{-1})	$\Delta S_D^{\ddagger}$ (J mol^{-1} K^{-1})
$Nb_{1.5}$-BEA	72 ± 3	−35 ± 21	45 ± 2	−91 ± 30

[a] Activation enthalpies and entropies were calculated from measured transition-state equilibrium constants ($K^{\ddagger}$, Fig. S13) and Eq. (23). Error in activation enthalpies and entropies was estimated by the linear regression analysis performed to fit the Eyring equation to the data in Fig. S13.

where $K_E^{\ddagger}$ and $K_D^{\ddagger}$ are the transition state equilibrium constants for $C_6H_{10}O$ formation and H_2O_2 decomposition, respectively. Expression of the rate of epoxidation and H_2O_2 decomposition in terms of the number of transition states (i.e., [Nb^{IV}-(O_2)-$C_6H_{10}^{\ddagger}$] or [Nb^{IV}-(O_2)-$H_2O_2^{\ddagger}$]), yields the following:

$$\frac{r_E}{[L]} = \frac{k_B T}{h}[Nb^{IV} - (O_2) - C_6H_{10}^{\ddagger}] \quad (19)$$

$$\frac{r_D}{[L]} = \frac{k_B T}{h}[Nb^{IV} - (O_2) - H_2O_2^{\ddagger}] \quad (20)$$

where T is the temperature in Kelvin, and k_B and h are Boltzmann's and Planck's constant, respectively. When the rates of reaction are measured on Nb^{IV}-(O_2)/Nb^{V}-(O_2) saturated surfaces, Eqs. (19) and (20) may be expressed in terms of reactant concentrations and transition-state equilibrium constants:

$$\frac{r_E}{[L]} = \frac{k_B T}{h}K_E^{\ddagger}[C_6H_{10}] \quad (21)$$

$$\frac{r_D}{[L]} = \frac{k_B T}{h}K_D^{\ddagger}[H_2O_2] \quad (22)$$

which allows the values of $K_E^{\ddagger}$ and $K_D^{\ddagger}$ to be determined by measuring the turnover rates for each reaction pathway at a given temperature. Values of $K_x^{\ddagger}$ may be expressed in terms of the apparent free energy change of activation ($\Delta G^{\ddagger}$), and subsequently $\Delta H^{\ddagger}$ and $\Delta S^{\ddagger}$ (from the relationship $\Delta G^{\ddagger} = \Delta H^{\ddagger} - T\Delta S^{\ddagger}$):

$$K_x^{\ddagger} = e^{-\Delta G_x^{\ddagger}/RT} = e^{-\Delta H_x^{\ddagger}/RT} e^{\Delta S_x^{\ddagger}/R} \quad (23)$$

where R is the ideal gas constant and the subscript x indicates that the associated variable corresponds to the formation of product x (i.e., epoxidation (E) for $C_6H_{10}O$ and decomposition (D) for H_2O). Fig. S13 shows measured values for $K_E^{\ddagger}$ and $K_D^{\ddagger}$ as functions of inverse temperature, which are used to determine experimental values for $\Delta H_E^{\ddagger}$, $\Delta H_D^{\ddagger}$, $\Delta S_E^{\ddagger}$, and $\Delta S_D^{\ddagger}$ by combining Eqs. (21)–(23).

Table 4 shows values of $\Delta H_E^{\ddagger}$, $\Delta H_D^{\ddagger}$, $\Delta S_E^{\ddagger}$, and $\Delta S_D^{\ddagger}$ for Nb-β calculated from $K_E^{\ddagger}$ and $K_D^{\ddagger}$ (Fig. S13, Eqs. (21) and (22)). $\Delta H^{\ddagger}$ values for epoxidation (72 kJ mol^{-1}) are 27 kJ mol^{-1} higher than for H_2O_2 decomposition (45 kJ mol^{-1}), which show that decomposition of H_2O_2 is enthalpically favored to that of C_6H_{10} epoxidation. Alternatively, $\Delta S^{\ddagger}$ values for H_2O_2 decomposition (−91 J mol^{-1} K^{-1}) are significantly more negative than for C_6H_{10} epoxidation (−35 J mol^{-1} K^{-1}), which makes epoxidation entropically favored in comparison to H_2O_2 decomposition. Interestingly, epoxidation is entropically favored over H_2O_2 decomposition, which suggests H_2O_2 selectivity is maximized by running the reaction at higher temperatures. This finding is not immediately intuitive as H_2O_2 and H_2O_2-derived intermediates are generally thought to decompose rapidly (in comparison to many other species) at elevated temperatures. Besides the non-intuitive differences in $\Delta H^{\ddagger}$, the selectivities for H_2O_2 to epoxidize C_6H_{10} reflect the ratio of the concentrations of the co-reactants (i.e., H_2O_2 or C_6H_{10}) for these bimolecular pathways, because the fate of the Nb^{IV}-(O_2) depends on the likelihood that this reactive intermediate first encounters liquid-phase C_6H_{10} or H_2O_2.

4. Conclusions

Ex situ XPS and in situ UV-vis and FTIR spectra reveal two types of metal-bound oxygen species (i.e., Nb^{IV}-(O_2) and Nb^{V}-(O_2)) that form upon the irreversible activation of H_2O_2 over Nb-β. Time-resolved UV-vis spectra acquired in situ reveal that Nb^{IV}-(O_2) (i.e., superoxide) species is responsible for olefin epoxidation, which is further confirmed by the isomeric distribution (cis:trans ~1) of the epoxide products from reaction with cis-stilbene. Collectively, these data, when combined with the observed dependencies of reaction rates on C_6H_{10}, H_2O_2, and $C_6H_{10}O$ provide a complete mechanistic understanding of olefin epoxidation over Nb-β that is consistent with an Eley-Rideal mechanism and indicate that the reactive form of oxygen (i.e., Nb^{IV}-(O_2)) forms irreversibly under reaction conditions. Additionally, this mechanism also accurately describes the dependence of epoxidation rates on reactant concentrations observed in previous studies on similar Ti- and Ta-based catalysts, which had assumed the quasi-equilibrated formation of the reactive intermediate. Calculated values of $\Delta H^{\ddagger}$ and $\Delta S^{\ddagger}$ for $C_6H_{10}O$ formation and H_2O_2 decomposition demonstrate that epoxide formation is enthalpically disfavored, which suggests that H_2O_2 selectivity toward epoxidation is maximized at higher temperatures. Overall, these results can aid in the rational design of increasingly selective catalysts for olefin epoxidation with H_2O_2 and provide methods to probe other metals to observe possible periodic trends in reactivity. Ongoing investigations in our group extend this mechanistic understanding of olefin epoxidation over M-β catalysts to the rational design of increasingly selective and active catalysts by probing periodic trends and the importance of the elemental identity of the substituted metal atom.

Acknowledgments

The authors acknowledge Ms. Megan Witzke and Mr. Neil Wilson for insightful discussions, feedback, and proofreading of the manuscript. We thank Dr. Damien Guironnet (UIUC) for use of equipment used in part for the synthesis of Nb-β, the preparation of H_2O_2-activated Nb-β, and ATR-IR for Nb-β and Si-β measurements. We thank Dr. Andre Sutrisno and the School of Chemical Sciences NMR lab for acquisition of the ^{1}H and ^{29}Si solid-state NMR spectra on Nb-β. We thank Dr. Rick Haasch for acquisition of the XPS spectra on Nb-β materials. This work was carried out in part in the Frederick Seitz Materials Research Laboratory Central Research Facilities, University of Illinois. DTB was supported in part by the National Defense Science and Engineering Graduate (NDSEG) Fellowship. This material is based upon work supported in part by, the U.S. Army Research Laboratory and the U. S. Army Research Office under grant number W911NF-16-1-0128, and upon work supported by the National Science Foundation grant number CBET-1553137.

Appendix A. Supplementary material

Additional catalyst characterization (p-XRD, DRUV-vis, solid-state NMR), Madon-Boudart criterion, detection of metal-bound oxygen species (in situ DRUV-vis and FTIR), MES-PSD data analysis derivation, derivation of previously proposed epoxidation and

H_2O_2-decomposition mechanisms, H_2O_2 selectivity data, temperature-dependence data. Supplementary data associated with this article can be found, in the online version, at http://dx.doi.org/10.1016/j.jcat.2017.02.008.

References

[1] W.J. Choi, C.Y. Choi, Production of chiral epoxides: epoxide hydrolase-catalyzed enantioselective hydrolysis, Biotechnol. Bioproc. Eng. 10 (2005) 167–179.
[2] D. Lehmhus, M. Busse, A. Herrmann, K. Kayvantash, Structural Materials and Processes in Transportation, Wiley-VCH, Germany, 2013.
[3] M. Subramanian, Polymer Testing: New Instrumental Methods, Momentum Press, New York, NY, 2012.
[4] E.V. Anslyn, D.A. Dougherty, Modern Physical Organic Chemistry, University Science, 2005.
[5] Allyl Compounds, in: Ullmann's Encyclopedia of Industrial Chemistry, Wiley-VCH, Weinheim, Germany, 2012.
[6] Epoxides, in: Ullmann's Encyclopedia of Industrial Chemistry, Wiley-VCH, Weinheim, Germany, 2012.
[7] G. Grigoropoulou, J.H. Clark, J.A. Elings, Recent developments on the epoxidation of alkenes using hydrogen peroxide as an oxidant, Green Chem. 5 (2003) 1–7.
[8] United States Environmental Protection Agency, Catalogue of Hazardous and Solid Waste Publications; Environmental Protection Agency, United States, 1992.
[9] W. Dilla, H. Dillenburg, H.G. Krebber, E. Ploenissen, Process for treating waste water containing organic and inorganic compounds, U.S. Patent 5478472, Dec 26, 1995.
[10] USP Technologies: How much does H_2O_2 cost? <http://www.h2o2.com/faqs/FaqDetail.aspx?fld=25> (accessed June 1, 2016).
[11] N.M. Wilson, D.T. Bregante, P. Priyadarshini, D.W. Flaherty, *Catalysis* 29 (2017) 122–212.
[12] C. De Ruiter, J.H. Wold, U.A. Brinkman, R.W. Frei, Design and evaluation of a sandwhich phase separation for on-line liquid/liquid extraction, Anal. Chim. Acta 192 (1987) 267–275.
[13] K. Backstrom, L.G. Danielsson, L. Nord, Design and evaluation of a new phase separator for liquid/liquid extraction in flow systems, Anal. Chim. Acta 169 (1985) 43–49.
[14] M.C.A. van Vliet, D. Mandelli, I.W.C.E. Arends, U. Schuchardt, R.A. Sheldon, Alumina: a cheap, active and selective catalyst for epoxidations with (aqueous) hydrogen peroxide, Green Chem. 3 (2001) 243–246.
[15] D. Mandelli, M.C.A. van Vliet, R.A. Sheldon, U. Schuchardt, Alumina-catalyzed alkene epoxidation with hydrogen peroxide, Appl. Catal., A 219 (2001) 209–213.
[16] R.L. Brutchey, D.A. Ruddy, L.K. Andersen, T.D. Tilley, Influence of surface modification of Ti-SBA15 catalysts on the epoxidation mechanism for cyclohexene with aqueous hydrogen peroxide, Langmuir 21 (2005) 9576–9583.
[17] I. Schmidt, A. Krogh, K. Wienberg, A. Carlsson, M. Brorson, C.J.H. Jacobsen, Catalytic epoxidation of alkenes with hydrogen peroxide over first mesoporous titanium-containing zeolite, Chem. Commun. (2000) 2157–2158.
[18] W. Fan, P. Wu, S. Namba, T. Tatsumi, Synthesis and catalytic properties of a new titanosilicate molecular sieve with the structure analogous to MWW-type lamellar precursor, J. Catal. 243 (2006) 183–191.
[19] D. Prasetyoko, Z. Ramli, S. Endud, H. Nur, Enhancement of catalytic activation of titanosilicalite-1 sulfated zirconia combination towards epoxidation of 1-octene with aqueous hydrogen peroxide, React. Kinet. Catal. Lett. 86 (2005) 83–89.
[20] N.E. Thornburg, A.B. Thompson, J.M. Notestein, Periodic trends in highly dispersed Groups IV and V supported metal oxide catalysts for alkene epoxidation with H_2O_2, ACS Catal. 5 (2015) 5077–5088.
[21] D.A. Ruddy, T.D. Tilley, Kinetics and mechanism of olefin epoxidation with aqueous H_2O_2 and a highly selective surface-modified TaSBA15 heterogeneous catalyst, J. Am. Chem. Soc. 130 (2008) 11088–11096.
[22] N. Morlanés, J.M. Notestein, Kinetic study of cyclooctene epoxidation with aqueous hydrogen peroxide over silica-supported calixarene–Ta(V), in: Appl. Catal. A l 387 (2010) 45–54.
[23] N. Morlanés, J.M. Notestein, Grafted Ta–calixarenes: tunable, selective catalysts for direct olefin epoxidation with aqueous hydrogen peroxide, J. Catal. 275 (2010) 191–201.
[24] I.D. Ivanchikova, N.V. Maksimchuk, I.Y. Skobelev, V.V. Kaichev, O.A. Kholdeeva, Mesoporous niobium-silicates prepared by evaporation-induced self-assembly as catalysts for selective oxidations with aqueous H_2O_2, J. Catal. 332 (2015) 138–148.
[25] A. Aronne, M. Turco, G. Bagnasco, G. Ramis, E. Santacesaria, M. Di Serio, E. Marenna, M. Bevilacqua, C. Cammarano, E. Fanelli, Gel derived niobium–silicon mixed oxides: characterization and catalytic activity for cyclooctene epoxidation, Appl. Catal. A: General 347 (2008) 179–185.
[26] F. Tielens, T. Shishido, S. Dzwigaj, What do the niobium framework sites look like in redox zeolites? A combined theoretical and experimental investigation, J. Phys. Chem. C 114 (2010) 3140–3147.
[27] C. Hammond, S. Conrad, I. Hermans, Simple and scalable preparation of highly active Lewis acidic Sn-beta, Angew. Chem. Int. Ed. Engl. 51 (2012) 11736–11739.
[28] Y. Wang, J.D. Lewis, Y. Román-Leshkov, Synthesis of itaconic acid ester analogues via self-aldol condensation of ethyl pyruvate catalyzed by hafnium BEA zeolites, ACS Catal. (2016) 2739–2744.
[29] W.R. Gunther, V.K. Michaelis, M.A. Caporini, R.G. Griffin, Y. Roman-Leshkov, Dynamic nuclear polarization NMR enables the analysis of Sn-Beta zeolite prepared with natural abundance (1)(1)(9)Sn precursors, J. Am. Chem. Soc. 136 (2014) 6219–6222.
[30] P. Wolf, C. Hammond, S. Conrad, I. Hermans, Post-synthetic preparation of Sn-, Ti- and Zr-beta: a facile route to water tolerant, highly active Lewis acidic zeolites, Dalton Trans. 43 (2014) 4514–4519.
[31] M.G. Clerici, P. Ingallina, Epoxidation of lower olefins with hydrogen peroxide and titanium silicalite, J. Catal. 140 (1993) 71–83.
[32] M.G. Clerici, G. Bellussi, U. Romano, Synthesis of propylene oxide from propylene and hydrogen peroxide catalyzed by titanium silicalite, J. Catal. 129 (1991) 159–167.
[33] T.A. Nijhuis, M. Makkee, J.A. Moulijn, B.M. Weckhuysen, The production of propene oxide: catalytic processes and recent developments, Ind. Eng. Chem. Res. 45 (2006) 3447–3459.
[34] E.L. First, C.E. Gounaris, J. Wei, C.A. Floudas, Computational characterization of zeolite porous networks: an automatec approach, Phys. Chem. Chem. Phys. 13 (2011) 17339–17358.
[35] C.B. Dartt, M.E. Davis, Characterization and catalytic activity of titanium containing SSZ-33 and aluminum-free zeolite beta, Appl. Catal., A 143 (1996) 53–73.
[36] B. Tang, W. Dai, X. Sun, N. Guan, L. Li, M. Hunger, A procedure for the preparation of Ti-Beta zeolites for catalytic epoxidation with hydrogen peroxide, Green Chem. 16 (2014) 2281.
[37] S. Dzwigaj, M.J. Peltre, P. Massiani, A. Davidson, M. Che, T. Sen, S. Sivasanker, Incorporation of vanadium species in a dealuminated b zeolite, Chem. Commun. 87–88 (1998).
[38] D.T. Bregante, D.W. Flaherty, Kinetic and Spectroscopic Evidence for Periodic Trends in Olefin Epoxidation over Supported Group IV and V Catalysts, 2017 (in review).
[39] H. Gao, G. Lu, J. Suo, S. Li, Epoxidation of allyl chloride with hydrogen peroxide catalyzed by titanium silicalite 1, Appl. Catal., A 138 (1996) 27.
[40] D.A. Ruddy, T.D. Tilley, Highly selective olefin epoxidation with aqueous H_2O_2 over surface-modified TaSBA15 prepared via the TMP method, Chem. Commun. 3350 (2007).
[41] A. Escobedo Morales, E. Sanchez Mora, U. Pal, Use of diffuse reflectance spectroscopy for optical characterization of un-supported nanostructures, in: Rev. Mex. Fis. E. 53 (2007) 18–22.
[42] Y. Zhao, X. Zhou, L. Ye, S.C.E. Tsang, Nanostructured Nb_2O_5 catalysts, Nano Rev. 3 (2012).
[43] S. Dzwigaj, Y. Millot, C. Méthivier, M. Che, Incorporation of Nb(V) into BEA zeolite investigated by XRD, NMR, IR, DR UV–vis, and XPS, Microporous Mesoporous Mater. 130 (2010) 162–166.
[44] V.L. Sushkevich, I.I. Ivanova, S. Tolborg, E. Taarning, Meerwein–Ponndorf–Verley–Oppenauer reaction of crotonaldehyde with ethanol over Zr-containing catalysts, J. Catal. 316 (2014) 121–129.
[45] S. Dzwigaj, Y. Millot, M. Che, Ta(V)-single site BEA zeolite by two-step postsynthesis method: preparation and characterization, Catal. Lett. 135 (2010) 169–174.
[46] International Zeolite Association: Verified Syntheses of Zeolitic Materials: Characterization by IR Spectroscopy. <http://www.iza-online.org/synthesis/VS_2ndEd/IR_Spectroscopy.htm> (accessed October 12, 2016).
[47] A. Corma, F.X. Llabrés i Xamena, C. Prestipino, M. Renz, S. Valencia, Water resistant, catalytically active nb and ta isolated lewis acid sites, homogeneously distributed by direct synthesis in a beta zeolite, J. Phys. Chem. C 113 (2009) 11306–11315.
[48] L.J. Burcham, J. Datka, I.E. Wachs, In situ vibrational spectroscopy studies of supported niobium oxide catalysts, J. Phys. Chem. B 103 (1999) 6015–6024.
[49] S. Roy, K. Bakhmutsky, E. Mahmoud, R.F. Lobo, R.J. Gorte, Probing Lewis acid sites in Sn-beta zeolite, ACS Catal. 3 (2013) 573–580.
[50] V.L. Sushkevich, A. Vimont, A. Travert, I.I. Ivanova, Spectroscopic evidence for open and closed lewis acid sites in ZrBEA zeolites, J. Phys. Chem. C 119 (2015) 17633–17639.
[51] J. Wang, V.F. Kispersky, W. Nicholas Delgass, F.H. Ribeiro, Determination of the Au active site and surface active species via operando transmission FTIR and isotopic transient experiments on 2.3 wt.% Au/TiO_2 for the WGS reaction, J. Catal. 289 (2012) 171–178.
[52] M. Boronat, P. Concepcion, A. Corma, M.T. Navarro, M. Renz, S. Valencia, Reactivity in the confined spaces of zeolites: the interplay between spectroscopy and theory to develop structure–activity relationships for catalysis, Phys. Chem. Chem. Phys. 11 (2009) 2876.
[53] A.N. Baga, A. Johnson, N.B. Nazhat, R.A. Saadalla-Nazhat, A simple spectrophotometric determination of hydrogen peroxide at low concentrations in aqueous solution, Anal. Chim. Acta 204 (1988) 349–353.
[54] N.M. Wilson, D.W. Flaherty, Mechanism for the direct synthesis of H_2O_2 on Pd clusters: heterolytic reaction pathways at the liquid-solid interface, J. Am. Chem. Soc. 138 (2016) 574–586.
[55] R.J. Madon, M. Boudart, Experimental criterion for the absence of artifacts in the measurement of rates of heterogeneous catalytic reactions, Ind. Eng. Chem. Fundam. 21 (1982) 438–447.

[56] G. Coudurier, C. Naccache, J.C. Vedrine, Uses of I.R. Spectroscopy in identifying ZSM zeolite structure, J. Chem. Soc. Chem. Commun. (1982) 1413–1415.
[57] H. Miessner, H. Kosslick, U. Lohse, B. Parlitz, V. Tuan, Characterization of highly dealuminated faujasite-type zeolites: ultrastable zeolite Y and ZSM-20, J. Phys. Chem. 97 (1993) 9741–9748.
[58] A. Urakawa, T. Bürgi, A. Baiker, Sensitivity enhancement and dynamic behavior analysis by modulation excitation spectroscopy: principle and application in heterogeneous catalysis, Chem. Eng. Sci. 63 (2008) 4902–4909.
[59] P.A. Giguere, K.B. Harvey, On the infrared absorption of water and heavy water in condense states, Can. J. Chem. 34 (1956) 798.
[60] W. Lin, H. Frei, Photochemical and FT-IR probing of the active site of hydrogen peroxide in Ti silicalite sieve, J. Am. Chem. Soc. 124 (2002) 9292–9298.
[61] S. Bordiga, A. Damin, F. Bonino, G. Ricchiardi, C. Lamberti, A. Zecchina, The structure of the peroxo species in the TS-1 catalyst as investigated by resonant Raman spectroscopy, Angew. Chem. Int. Ed. Engl. 41 (2002) 4734.
[62] C. Chen, H. Yuan, H. Wang, Y. Yao, W. Ma, J. Chen, Z. Hou, Highly efficient epoxidation of allylic alcohols with hydrogen peroxide catalyzed by peroxoniobate-based ionic liquids, ACS Catal. 6 (2016) 3354–3364.
[63] B. Notari, Microporous crystalline titanium silicates, Adv. Catal. 41 (1996) 253–334.
[64] J.J. Bravo-Suárez, K.K. Bando, J. Lu, M. Haruta, T. Fujitani, S.T. Oyama, Transient technique for identification of true reaction intermediates: hydroperoxide species in propylene epoxidation on gold/titanosilicate catalysts by X-ray absorption fine structure spectroscopy, J. Phys. Chem. C 112 (2008) 1115–1123.
[65] F. Bonino, A. Damin, G. Ricchiardi, M. Ricci, G. Spano, R. D'Aloisio, A. Zecchina, C. Lamberti, C. Prestipino, S. Bordiga, Ti-peroxo species in the Ts-1/H_2O_2/H_2O system, J. Phys. Chem. B 108 (2008) 3573–3583.
[66] D. Srinivas, P. Manikandan, S.C. Laha, R. Kumar, P. Ratnasamy, Reactive oxo-titanium species in titanosilicate molecular sieves: EPR investigations and structure–activity correlations, J. Catal. 217 (2003) 160–171.
[67] V.N. Shetti, P. Manikandan, D. Srinivas, P. Ratnasamy, Reactive oxygen species in epoxidation reactions over titanosilicate molecular sieves, J. Catal. 216 (2003) 461–467.
[68] L. Wang, G. Xiong, J. Su, P. Li, H. Guo, In situ UV Raman spectroscopic study on the reaction intermediates for propylene epoxidation on TS-1, J. Phys. Chem. C 116 (2012) 9122–9131.
[69] M. Ziolek, I. Sobczak, P. Decyk, K. Sobańska, P. Pietrzyk, Z. Sojka, Search for reactive intermediates in catalytic oxidation with hydrogen peroxide over amorphous niobium(V) and tantalum(V) oxides, Appl. Catal. B 164 (2015) 288–296.
[70] J. Guzman, S. Carrettin, A. Corma, Spectroscopic evidence for the supploy of reactive oxygen during CO oxidation, J. Am. Chem. Soc. 127 (2005) 3286.
[71] R.Q. Long, H.L. Wan, In situ confocal microprobe Raman spectroscopy study of CeO_2 catalyst for the oxidative coupling of methane, J. Chem. Soc., Faraday Trans. 93 (1997) 355.
[72] M. Nakayama, M. Xue, W. An, P. Liu, M.G. White, Influence of cluster-support interactions on reactivity of size-selected NbxOy clusters, J. Phys. Chem. C 119 (2015) 14756–14768.
[73] J.F. Marco, J.R. Gancedo, F.J. Berry, The oxidation states of titanium and niobium in compounds of composition $Sn_xNbTiP_3O_{12}$ ($O < x < 0.5$): an XPS study, Polyhedron 16 (1997) 2957–2961.
[74] S.E. Stein, IR and Mass Spectra, in: W.G. Mallard, P.J. Linstrom (Eds.), NIST Chemistry WebBook, NIST Standard Reference Database Number 69; National Institute of Standards and Technology: Gaithersburg, MD, (February) 2000, Acetonitrile, Cyclohexene, and Cyclohexane (http://webbook.nist.gov).
[75] N.K.K. Raj, A.V. Ramaswamy, P. Manikandan, Oxidation of norbornene over vanadium-substituted phosphomolybdic acid catalysts and spectroscopic investigations, J. Mol. Catal. A: Chem. 227 (2005) 37–45.
[76] C.K. Sams, K.A. Jorgensen, Mechanistic aspects of vanadium-catalysed oxygen transfer reactions, Acta Chem. Scand. 49 (1995) 839–847.
[77] R.V. Ottenbacher, D.G. Samsonenko, E.P. Talsi, K.P. Bryliakov, Enantioselective epoxidations of olefins with various oxidants on bioinspired mn complexes: evidence for different mechanisms and chiral additive amplification, ACS Catal. 6 (2016) 979–988.
[78] Zeolyst: Zeolite Beta. <http://www.zeolyst.com/our-products/standard-zeolite-powders/zeolite-beta.aspx> (accessed June 1, 2016).
[79] D. Murzin, Engineering Catalysis, de Gruyter, Gottingen, Germany, 2013.
[80] L. Arnaut, S. Formosinho, H. Burrows, Chemical Kinetics: From Molecular Structure to Chemical Reactivity, Elsevier, Netherlands, 2007.
[81] D.W. Flaherty, E. Iglesia, Transition-state enthalpy and entropy effects on reactivity and selectivity in hydrogenolysis of n-alkanes, J. Am. Chem. Soc. 135 (2013) 18586–18599.